University of Alberta

GENERATION, PROPAGATION AND BREAKING OF AN INTERNAL GRAVITY WAVE BEAM

by

Heather A. Clark

A thesis submitted to the Faculty of Graduate Studies and Research in partial fulfillment of the requirements for the degree of

Master of Science

Department of Physics

Spring 2010
Edmonton, Alberta

Examining Committee

Bruce Sutherland, Physics & Earth and Atmospheric Sciences

Morris Flynn, Mechanical Engineering

Moritz Heimpel, Physics

Gordon Swaters, Mathematical and Statistical Sciences

Abstract

We report upon an experimental study of internal gravity waves generated by the large-amplitude vertical oscillations of a circular cylinder in uniformly stratified fluid. Quantitative measurements are performed using a modified synthetic schlieren technique for strongly stratified solutions of NaCl or NaI. Oscillatory turbulent patches that develop around the cylinder are found to be the primary source of the observed quasi-monochromatic wave beams whose characteristics differ from theoretical predictions and experimental investigations of waves generated by small-amplitude cylinder oscillations. Over long times the waves break down into turbulence that is examined quantitatively through conductivity probe measurements and qualitatively through unprocessed synthetic schlieren images. Based on observations of the location of wave breakdown we determine that the likely mechanism for breakdown is through parametric subharmonic instability. This conclusion is supported by fully nonlinear numerical simulations of the evolution of a temporally monochromatic internal wave beam.

Acknowledgements

It has been a privilege to work under the supervision of Dr. Bruce Sutherland, whose recognized abilities in science and research are matched by his gift with students. Bruce is genuinely excited about the endeavours and accomplishments of his graduate students in professional and personal arenas, and he has fostered my development in both respects. I would also like to thank all members of my committee for their comments on my thesis, as well as their influence in my direction through teaching.

I am fortunate to have colleagues as talented and sociable as the members of my research group. Kate, your companionship during this process has been a simultaneously uplifting and grounding force. I will dearly miss your presence at the neighbouring desk as we take on our next challenges separately.

My sincerest thanks to everyone who has remained beside me through the diagnosis of Celiac Disease and my ongoing return to health. Your help and understanding have been crucial to the completion of my program.

My family and my boyfriend have been unwavering sources of support and encouragement during this degree. They have shared in trials and joys, both personal and academic. I want to thank my parents for their gentle guidance and their expression of confidence in my abilities and my judgment. Kevin, your patience and strength have borne me through more challenges in the past few years than I can possibly list.

Finally, I would like to acknowledge the significant financial contributions of NSERC and the Alberta Ingenuity Fund.

Table of Contents

List of Tables

List of Figures

Chapter 1

Introduction

Density stratified fluids support the propagation of internal gravity waves that arise from buoyancy restoring forces. The internal waves exist at frequencies below the buoyancy (Brunt-Väisälä) frequency of the stratification, at which the oscillations of the fluid are purely in the vertical direction. Energy and momentum are transported in geophysical fluids by the internal waves radiating from localized sources. Observations, modelling, and experiments have been used to study in detail several generation mechanisms and the properties of the resulting waves. In particular, topographic forcing by tidal flow over features of the ocean floor is observed to be a major source of oceanic internal waves (Rudnick et al., 2003; St. Laurent et al., 2003; Lamb, 2004) that are subsequently responsible for significant diapycnal mixing (St. Laurent and Garrett, 2002). Similarly, flow over mountains may generate moderate- to large-amplitude atmospheric waves (Chan et al., 1993), the turbulent breakdown of which has been observed directly through in-flight measurements (Lilly and Lester, 1974). Fritts and Alexander (2003) reviewed the generation of atmospheric internal waves by several primary sources, including topography, convection, shear, geostrophic adjustment and wave-wave interactions. During the process of geostrophic adjustment, excess energy is radiated in the form of inertial waves as geostrophically balanced flow conditions are restored

(Fritts and Alexander, 2003). Using atmospheric data collected during commercial flights, Fritts and Nastrom (1992) examined the relative importance of several of the primary atmospheric generation mechanisms. It was found that topographic forcing was responsible for the largest enhancement of velocity and temperature variance relative to regions with no source of waves. In general, the existence of such disturbances in the atmosphere and oceans can have a significant nonlocal effect on the mean flow through the propagation and breaking of internal waves.

It has been noted previously (Sutherland, 2006a) that much observational work on internal waves has focused on the low frequency, low wavenumber components of the wave spectrum. The observation of such waves is favoured by the timescales and lengthscales associated with current measurement techniques. In addition, studies are motivated by measured geophysical spectra that exhibit a concentration of wave power at low frequencies. In the ocean this corresponds to tidal forcing of waves, while in the atmosphere the majority of the momentum flux from topographic generation is due to waves with horizontal wavelengths between approximately 10 and 100 kilometres (Fritts and Alexander, 2003). While a significant fraction of the total internal wave energy may be at low frequencies, the cumulative effects of disturbances with higher frequencies and wavenumbers may be non-negligible (Sutherland, 2006a). In this work we focus upon a generation mechanism that is applicable to the upper range of the internal wave spectrum.

Previous studies of internal wave generation by turbulence have been motivated by such phenomena as stationary turbulence (Linden, 1975), wind stress on the ocean producing a sheared turbulent mixed layer (Munroe and Sutherland, 2008), turbulent shear flow over a barrier (Sutherland and Linden, 1998), and the turbulent wake in the lee of topography (Aguilar and Sutherland, 2006). While turbulent flows are involved to varying extent in geophysical sources of internal waves, the generation process is currently not well understood. It has been observed in experiments (Sutherland and Linden, 1998; Dohan and Sutherland, 2003; Aguilar and Sutherland, 2006) and numerical simulations (Diamessis et al., 2005) that turbulent sources generate waves in a narrow frequency range relative to the background buoyancy frequency. In a recent numerical study, Taylor and Sarkar (2007) found that the internal waves generated by oceanic bottom boundary layer turbulence propagated at angles between 35 and 60 degrees from the vertical. It was shown that linear differential viscous decay could produce the observed spectral peak and decay in wave amplitudes: small-scale waves or those with high or low frequencies decayed more rapidly in their simulations. However, the proposed model may not be an adequate explanation in the case of larger amplitude waves (Taylor and Sarkar, 2007). A key difference between the numerics and experiments is that the former used large-eddy simulation for the numerical boundary layer and so did not resolve finescale turbulence. Although a theoretical viscous model was in agreement with the results of the simulations, experiments show the immediate generation of narrow-band internal waves on a timescale that is less than that required for differential viscous decay.

The generation of internal waves by a small-amplitude monochromatic localized source has been studied extensively in theory (Makarov et al., 1990; Voisin, 1991). In particular, Hurley and Keady (1997) presented an approximate solution for Boussinesq waves generated by a cylinder oscillating at small amplitude in a viscous fluid. Theory predicts that four wave beams emanate at a fixed angle to the vertical from the cylinder in a “St. Andrew’s Cross” pattern (Voisin, 1991). The angle is set by the frequency of oscillation of the cylinder relative to the buoyancy frequency, with the beams approaching the vertical as the frequency increases. The beams are predicted to exhibit a bimodal amplitude structure near the source, and a unimodal structure evolves far from the cylinder due to viscous attenuation (Makarov et al., 1990). Moderate-amplitude forcing in Boussinesq fluids has been investigated in laboratory experiments by Sutherland et al. (1999) and Sutherland and Linden (2002) with circular and elliptical cylinders, respectively. In general, good qualitative agreement was found between the experiments and the linear, viscous, Boussinesq theory of Hurley and Keady (1997). However, the beam width was consistently underpredicted because the theory neglected the formation of a viscous boundary layer around the cylinder. The current work is focused on the study of internal waves generated by large-amplitude oscillations of a circular cylinder in a strongly stratified fluid. Boundary layer separation resulted from the large-amplitude forcing, so that the internal waves were launched effectively by an oscillatory turbulent patch. In this sense, the extension of previous experimental work to include large-amplitude effects also alters the generation process.

Although the region bounding the cylinder is turbulent, we anticipate that the source of waves retains a dominant frequency due to the oscillatory forcing of the turbulent patch. Therefore, it differs from previous work examining the generation of waves by an oscillating grid (Linden, 1975; Dohan and Sutherland, 2003) in which the approximately homogeneous turbulence had a broad frequency spectrum. This work includes cylinder frequencies below the buoyancy frequency, whereas the frequency of grid oscillations in the cited “mixing box” experiments was above the buoyancy frequency in all cases. The source conditions also differ due to the spatial localization of the turbulent patch rather than the horizontally uniform conditions of previous studies.

As well as standard sodium chloride (NaCl) solutions, a new experimental technique (Clark and Sutherland, 2009) that is applied in this work is the use of sodium iodide (NaI) to produce stronger stratifications and thus higher buoyancy frequencies than those in conventional tank experiments with NaCl.

The solubility of NaI at room temperature is higher than that for NaCl, so a larger density gradient can be achieved over a given tank depth. Whereas typical stratifications have a density change on the order of 5% over the depth of the fluid, the density differences in this study are approximately 20% for solutions of NaCl and 50% for NaI. The large density gradients introduce the potential for non-Boussinesq growth of the wave amplitude with height, which is a consequence of momentum conservation as the ambient density decreases in the vertical. Such effects could have an observable influence on the propagating beams.

Presently, the parameterization of internal wave dynamics in atmospheric General Circulation Models is based largely upon linear theory. Heuristics are used to predict the amplitude at which waves are generated and the height at which they break, either as a result of encountering a critical level or due to anelastic (analogous to non-Boussinesq) growth. Recent numerical and theoretical work (Sutherland, 2006b) has questioned the use of these linear theory heuristics by showing that weakly nonlinear effects can either enhance or retard the amplitude growth of an internal wavepacket. While the large-amplitude forcing in our experiments acts to modify the source region by causing boundary layer separation, it also has the effect of generating finite-amplitude waves. Thus, we anticipate that nonlinear effects may have a non-negligible influence on the evolution of the wave beams. Tabaei and Akylas (2003) showed through an asymptotic analysis that nonlinear effects are relatively insignificant for an isolated beam with slow along-beam modulations in a uniform, Boussinesq stratification. Dispersive and viscous effects were found to be the dominant factors in determining the propagation of isolated beams. A subsequent paper (Tabaei et al., 2005) investigated the role of nonlinearity in situations where there exists a region of interaction, namely the reflection of a wave beam from a slope or the collision of two beams. In such cases it was found that nonlinear effects result in the generation of higher-harmonic beams that propagate out of the interaction region and into the far field. In this study we find that nonlinear effects have a significant influence on the evolution of the moderate-amplitude waves, resulting in wave breaking and turbulent mixing of a single beam in the absence of critical layers. The instability mechanism requires investigation, particularly in light of existing theoretical predictions about the relative unimportance of nonlinear considerations for an isolated beam (Tabaei et al., 2005).

1.1 Thesis Overview

Chapter 2 describes the experimental apparatus and the implementation of the synthetic schlieren measurement technique in strongly stratified fluids. Measurements of the optical properties of NaI solutions are presented for this purpose[1]. A derivation of the equations for Boussinesq schlieren is provided in Appendix B. In Chapter 3 we provide a detailed description of the analysis methods that are used to obtain the wave frequency, lengthscale and amplitude at relatively early times following generation. From these measured properties we also compute the power of the primary beam. Each quantity is compared to linear theory predictions in order to assess the relative effects of the turbulent generation mechanism observed in experiments. Appendix A is a review of this linear theory, based on the work of Hurley and Keady (1997).

Chapter 4 contains the results of the examination of the observed beam instabilities and breakdown. We describe a qualitative method for the determination of breakdown time and location relative to the position of the cylinder. Fully nonlinear numerical simulations of a monochromatic wave beam are performed to test our hypothesis for the instability mechanism[2]. A summary of

---

[1] A version of this chapter has been published. H. A. Clark and Bruce R. Sutherland (2009). *Experiments in Fluids*. 47:183-193.

[2] A version of Chapters 3 and 4 has been submitted for publication. Heather A. Clark

the significant findings of this thesis is given in Chapter 5.

---

and Bruce R. Sutherland. *Physics of Fluids*.

Chapter 2

Experimental Methods

2.1 Introduction

The majority of internal wave experiments to date have used stratified solutions of NaCl to obtain Boussinesq conditions in a laboratory setting. In such cases the maximum density change over the depth of a fluid is limited by the saturation density at typical ambient conditions. However, in general this limit is not approached because the desired density gradient is achieved at much lower concentrations. Part of the motivation for the work of this thesis is to introduce more significant density variations over the vertical scale of wave propagation and measurement. For this reason, experiments using NaCl were performed in stratifications ranging from near-saturation to near-fresh concentrations. In addition, this work also includes the first use of NaI stratifications to achieve larger density gradients than in previous experiments. The experiments were performed in the laboratory of Paul F. Linden at the Department of Mechanical and Aerospace Engineering, University of California, San Diego.

This chapter begins with a description of the experimental apparatus and measurements of characteristic background density profiles in Section 2.2. In Section 2.3 we present the modified form of the synthetic schlieren equations, which are used to obtain quantitative measurements of the wave properties from video recordings of the experiments. To implement synthetic schlieren in strongly stratified fluids, the dependence of the index of refraction upon the fluid density is required. The results of experimental measurements of this relationship for solutions of NaI are the topic of Section 2.4.

2.2 Apparatus and Density Stratifications

We have performed a series of experiments using an oscillating cylinder to generate waves in strong stratifications of NaCl or NaI solutions. As illustrated schematically in Figure 2.1, a cylinder of radius R_c was forced by a variable-speed motor to produce vertical oscillations with half peak-to-peak amplitude A_c and angular frequency ω_c in a rectangular acrylic tank. In order to obtain disturbances that were uniform in the spanwise (y) direction, the length of the cylinder was 2 mm less than the inner separation of the tank walls. The tank of dimensions $W_t = 122.3\,\mathrm{cm}$ and $L_t = 15.5\,\mathrm{cm}$ was filled to a depth of $H_t \simeq 55\,\mathrm{cm}$. For both types of stratification, experiments were performed with the cylinder centred approximately 12 cm above the bottom of the tank or approximately 8 cm below the fluid surface. This was done to allow for a comparison between the characteristics of upward- and downward-propagating waves. The spatial region for quantitative analysis was focused to one side of the cylinder, as we assume symmetry of the wave properties about the vertical axis. As in the case of small-amplitude forcing, four wave beams were observed emanating from the source region. Hereafter we will refer to the “primary beam” and the “reflected beam” as they are shown in Figure 2.1. The terms are used similarly for the case with the cylinder near the top of the tank, but the beam reflection occurs off of the fluid surface rather than the bottom of the tank.

A standard double bucket apparatus (Oster, 1965) was used to produce the NaCl stratifications with a near-saturation density at the bottom of the tank. For NaI solutions, 2 cm deep layers of decreasing density from bottom to

(a) Front View

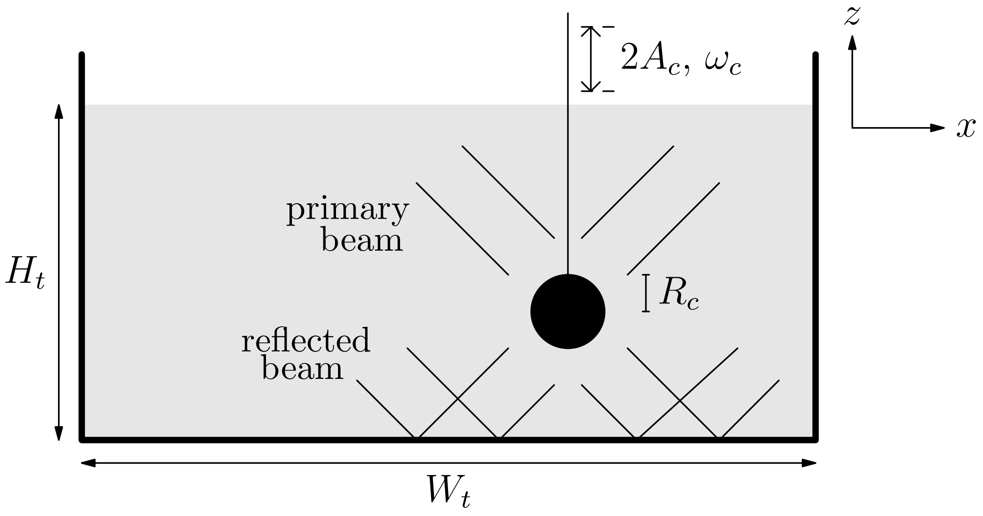

(b) Side View

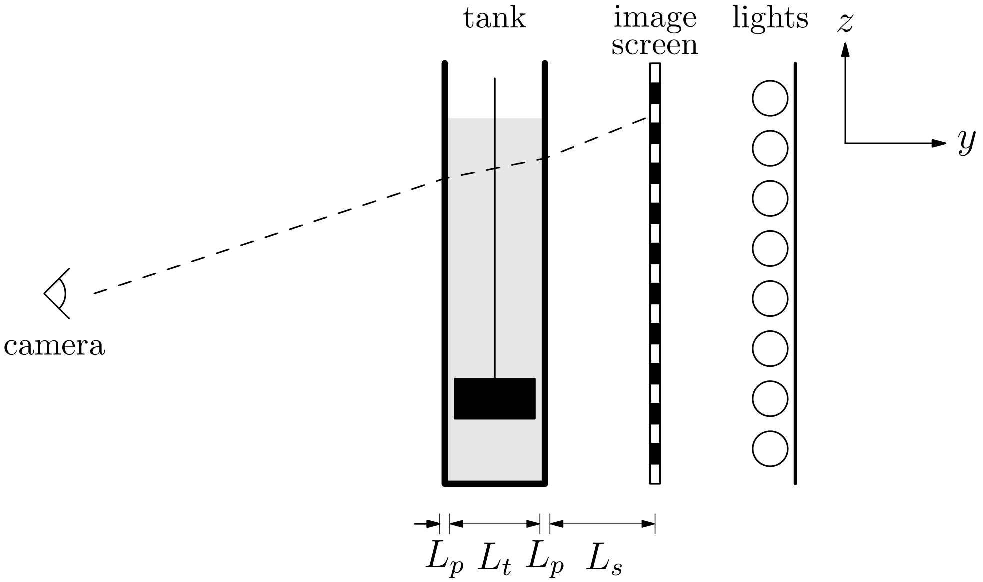

Figure 2.1: (a) Schematic diagram of the suspended cylinder oscillating with constant frequency and amplitude. An approximate resulting wave beam pattern is shown. (b) A side view of the synthetic schlieren apparatus. The dashed line represents the path of a light ray from the screen to the camera.

top were successively manually poured through a sponge float and the system was allowed to diffuse overnight. The dilution for each layer was performed with the target density calculated to result in an exponential decrease. For the experiments reported upon here, the maximum density at the tank bottom was approximately $1.5\,\mathrm{g/cm^3}$. For both solutions, the resulting density profile was established such that the fluid could be treated as an approximately uniformly stratified non-Boussinesq fluid, for which the background density profile, $\bar{\rho}(z)$, decreased exponentially with height:

$$\bar{\rho}(z) = \rho_0 \exp[-(z - z_0)/H\,]\,, \tag{2.1}$$

where z_0 is a reference height at which the density, ρ_0, is known, and H is the density scale height. A conductivity probe was used to traverse the upper 45 cm of the tank, making approximately 40 measurements of the fluid density per vertical centimeter between the surface and 10 cm above the tank bottom. The data, shown in Figure 2.2 for characteristic experiments, were fitted with an exponential function of the form of (2.1) using a least-squares method. $H \simeq 270\,\mathrm{cm}$ for NaCl stratifications, and $H \simeq 130\,\mathrm{cm}$ for experiments using NaI. To account for the large variations in density over the depth of the fluid, we calculate the background buoyancy frequency, N, using the non-Boussinesq relation,

$$N^2(z) = -\frac{g}{\bar{\rho}}\frac{d\bar{\rho}}{dz}, \tag{2.2}$$

where g is the acceleration due to gravity. Given the non-Boussinesq form of the equation, the construction of near-exponential stratifications in the experiments results in an approximately constant background buoyancy frequency denoted by N_0. The values of H shown above yield buoyancy frequencies of $N_0 \simeq 1.9\,\mathrm{s}^{-1}$ and $N_0 \simeq 2.7\,\mathrm{s}^{-1}$ for NaCl and NaI, respectively, according to (2.2).

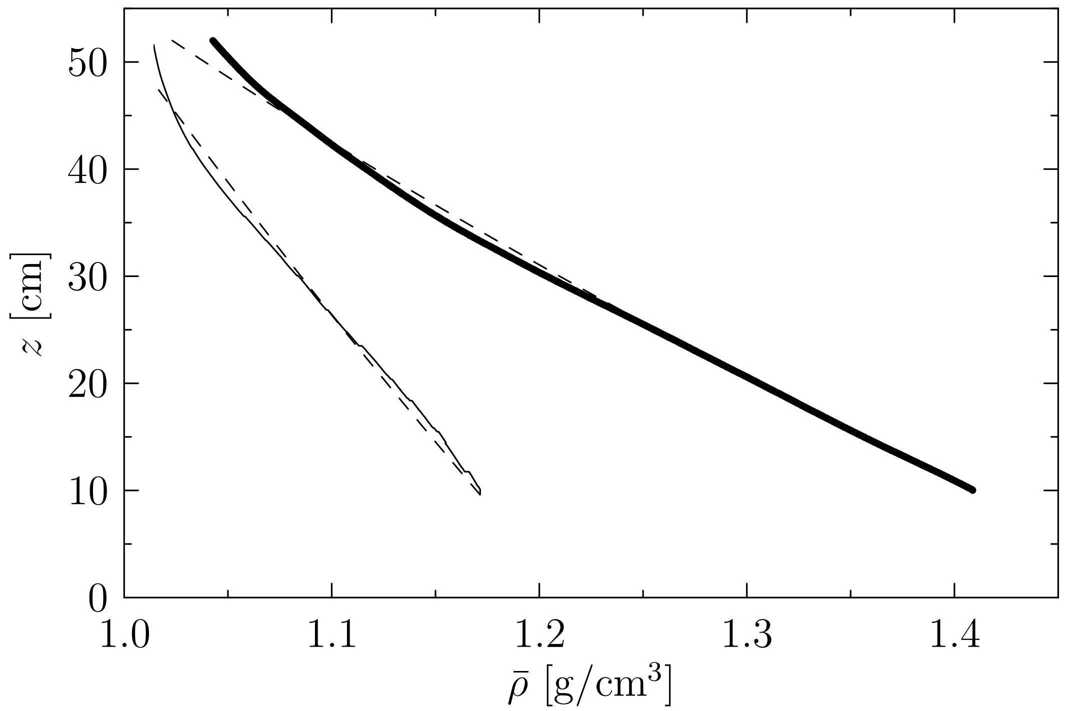

Figure 2.2: Vertical fluid density profile for typical experiments using NaCl (thin solid curve) and NaI (thick solid curve). Dashed curves are the exponential fits to experimental data.

We have calculated the Reynolds number, Re, using a velocity scale of $A_c\,\omega_c$ and a length scale of $2R_c$. Measurements of the viscosity of NaI solutions at a temperature of 20.005°C were performed using an Anton Paar DMA 500 density meter, with densities between that of fresh water and approximately $1.6\,\mathrm{g/cm^3}$. We find that for these densities the kinematic viscosity, ν, lies in the range of $0.01\,\mathrm{cm^2/s}$ to $0.016\,\mathrm{cm^2/s}$. If we assume similar viscosities for solutions of NaCl up to saturation densities, we may estimate a range of Re for the experiments based on the forcing parameters. We obtain $\mathrm{Re} \approx 250 - 4400$ across the entire forcing parameter space, but the experiments that will be of focus in Chapter 3 lie in the more intermediate values of $\mathrm{Re} \approx 1500 - 2000$.

A Cohu CCD video camera positioned 465 cm from the front of the tank was focused on an image of horizontal black lines situated $L_s = 15.5\,\mathrm{cm}$ behind the rear tank wall (Fig. 2.1(b)). The image screen was back-illuminated by a set of regularly spaced fluorescent tubes. The field of view was a region spanning the depth of the tank and approximately 70 cm in the x direction with the cylinder situated near the corner of the image. Video images were recorded on SVHS tape at a rate of 1 frame per 1/30 seconds and were subsequently digitized with a spatial resolution of approximately 0.12 cm using the software package DigImage (Dalziel, 1992). The images were then processed to determine the amplitude of generated waves through a technique known as synthetic schlieren. This method and its adaption for strongly stratified fluids is described in the following section.

2.3 Synthetic Schlieren

Here we briefly review quantitative synthetic schlieren as presented by Sutherland et al. (1999) and indicate where modifications should be made for a strong density stratification or non-Boussinesq fluid. A derivation of the synthetic schlieren equations for Boussinesq stratifications is given in Appendix B.

Propagating waves displace the isopycnal surfaces, resulting in variations of the local density gradient. This changes the local index of refraction in space and time, thereby affecting the degree to which light passing through the tank is deflected. By measuring the apparent displacements of objects (lines or dots) in the image behind the tank, one can calculate the perturbation density gradient associated with spanwise-uniform waves. From this, other wave fields may be determined.

To perform this calculation, we assume that the background index of refraction, $\bar{n}$, is a quadratic function of the background density of the salt solution and we form an expansion about a reference density ρ_0:

$$\bar{n}(\bar{\rho}) = n_0 + a_1(\bar{\rho} - \rho_0) + \frac{1}{2} a_2(\bar{\rho} - \rho_0)^2, \tag{2.3}$$

where

$$a_1 = \left.\frac{d\bar{n}}{d\bar{\rho}}\right|_{\rho_0} \quad \text{and} \quad a_2 = \left.\frac{d^2\bar{n}}{d\bar{\rho}^2}\right|_{\rho_0} \tag{2.4}$$

are empirically measured constants. Taking $\rho_0 = 0.99823\,\mathrm{g/cm^3}$ to be the density of fresh water at room temperature, the reference index of refraction is $n_0 = 1.3330$.

As a light ray traverses the width of the tank at a small angle from the horizontal, it encounters a vertical gradient in the index of refraction, so that the ray follows an approximately parabolic path (Sutherland et al., 1999). The curvature of the path is proportional to the density gradient at that vertical level in the fluid. By measuring the vertical deflection, Δz, of an image one can compute the density gradient and thus the change to the squared buoyancy frequency,

$$\Delta N^2 \simeq -\Delta z\,\frac{1}{\gamma}\left[\frac{1}{2}L_t^2 + L_t\,\bar{n}\left(\frac{L_p}{n_p} + \frac{L_s}{n_a}\right)\right]^{-1}, \tag{2.5}$$

in which $n_p = 1.49$ and $n_a = 1.0$ are the refractive indices of acrylic and air. Here we have expressed the vertical gradient in the index of refraction in terms of the buoyancy frequency as

$$\frac{\partial\bar{n}}{\partial z} = \frac{d\bar{n}}{d\bar{\rho}}\frac{\partial\bar{\rho}}{\partial z} = -\left(\frac{1}{g}\frac{\bar{\rho}}{\bar{n}}\frac{d\bar{n}}{d\bar{\rho}}\right)\bar{n}N^2 = -\gamma\bar{n}N^2, \tag{2.6}$$

so that the quantity γ in (2.5) is given by

$$\gamma = \frac{1}{g}\frac{\bar{\rho}}{\bar{n}}\frac{d\bar{n}}{d\bar{\rho}} = \frac{1}{g}\frac{\bar{\rho}}{\bar{n}}[a_1 + a_2(\bar{\rho} - \rho_0)]. \tag{2.7}$$

The calculation of ΔN^2 from Δz differs from previous work (Sutherland et al., 1999; Dalziel et al., 2000) in the definition of γ. In that work it was assumed that $\gamma = \frac{1}{g}\frac{\rho_0}{n_0}a_1$, a constant. Here, to account for significant variations of the background density and index of refraction with height, both quantities are taken to be functions of z. The quadratic variation of $\bar{n}$ with $\bar{\rho}$, through the nonzero value of a_2 in (2.3), is also included. Further discussion of these modifications to synthetic schlieren can be found in Section 2.4.

The apparent vertical deflection is determined using changes in pixel intensities of the digitized image in the same manner as reported in Sutherland et al. (1999). By measuring Δz variations between small times (typically 2/30 s), the time derivative can be estimated. From this, using (2.5) with Δz replaced by $\partial z/\partial t$, one can measure the rate of change of the buoyancy frequency, N_t^2, due to the stretching and compressing of isopycnals by waves.

2.4 Optical Properties of NaI Solutions

Conventional experiments with stratified fluids use NaCl solutions of varying density, the properties of which are well documented (Weast, 1981). In particular, the dashed lines in Figure 2.3 plot the dependence of $\bar{n}$ on $\bar{\rho}$ and of $\bar{\rho}$ on concentration, c, of the solution. For NaCl the curves extend to densities of $\bar{\rho} \simeq 1.2\,\mathrm{g/cm^3}$, at which the solutions are saturated at approximately 20°C. Using tabulated data of $\bar{n}$ and $\bar{\rho}$ from Weast (1981) for solutions of NaCl we find that for a profile of the form of (2.3), $a_1 = 0.2458\,\mathrm{cm^3/g}$ and $a_2 = -0.1208\,\mathrm{cm^6/g^2}$. These values are used in (2.5) and (2.7) for the calculation of ΔN^2 and N_t^2 in experiments with stratifications of NaCl solutions. Assuming a stratification such that $\bar{\rho} \in [0.99823, 1.2]\,\mathrm{g/cm^3}$, the variation in γ over depth is approximately 5%. For the value of γ calculated using the maximum density and the corresponding index of refraction, the a_2 term contributes 11% of the total. Thus the inclusion of the nonlinear term in (2.3) has a non-negligible effect for solutions of NaCl as saturation densities are approached.

While there are tabulated data of the optical properties of NaCl solutions, to our knowledge there is no analogous information for NaI available in the literature. We have therefore performed measurements relating the concentra-

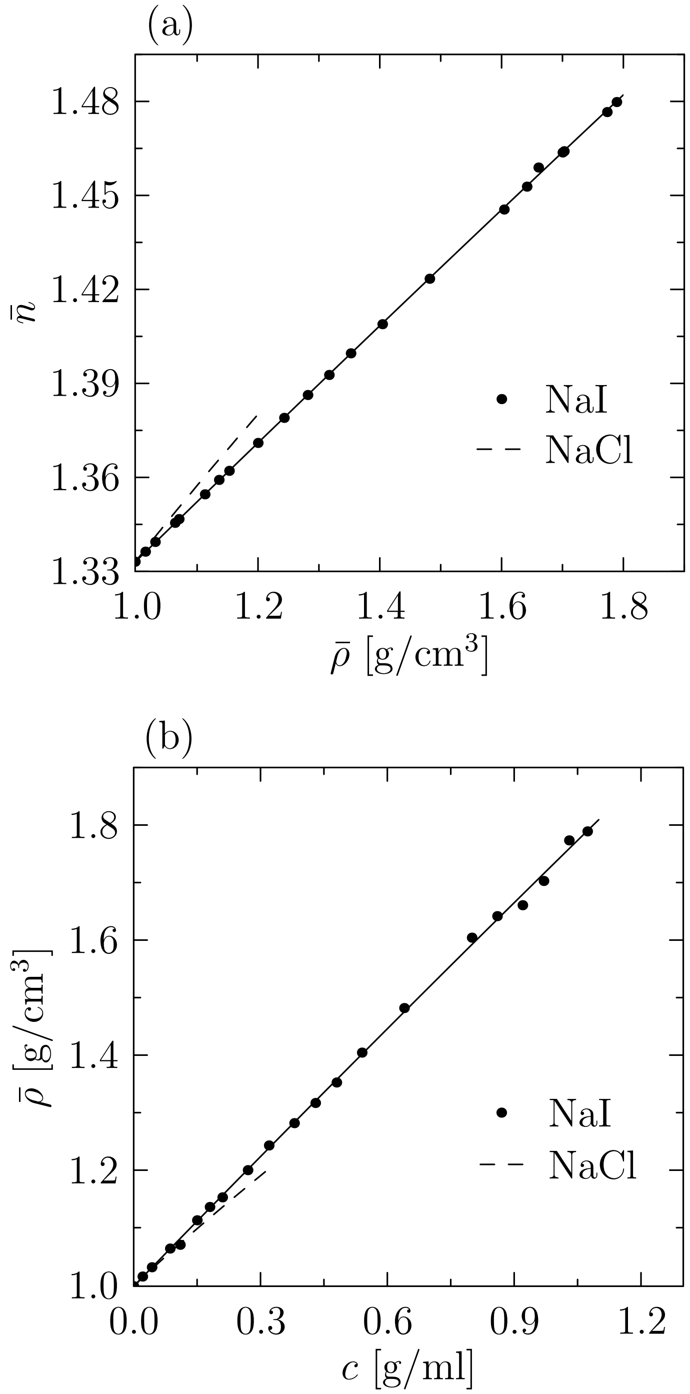

Figure 2.3: (a) The measured index of refraction (solid circles) as a function of density of NaI in solution. The quadratic fit is shown as a solid line. (b) Measurements of density (solid circles) as a function of concentration. The data for NaCl (dashed lines) have been included in both plots for comparison.

tion, density, and index of refraction of NaI solutions. The index of refraction of solutions with known concentrations was measured at a temperature of 21.0 ± 0.5°C using a Bausch & Lomb Abbe-3L refractometer. The corresponding density for each solution was measured at 20.00°C with an Anton Paar DMA 4500 density meter. We assume that temperature variations on the order of 1°C will not affect the index of refraction at the level of accuracy of our measurements. The results are shown as the solid circles in Figure 2.3 for densities ranging up to approximately $1.8\,\mathrm{g/cm^3}$, which corresponds to a solution of approximately 50% NaI by weight. The measurements have been fit with quadratic functions, shown as solid lines.

Using $n_0 = 1.3330$ and $\rho_0 = 0.99823\,\mathrm{g/cm^3}$, we find that the coefficients in the index of refraction as a function of density, (2.3), for NaI solutions are

$$a_1 = 0.1894 \pm 0.0002\,\mathrm{cm^3/g} \text{ and } a_2 = -0.0086 \pm 0.0006\,\mathrm{cm^6/g^2}. \qquad (2.8)$$

Note that the nonlinear variation of the index of refraction with density is much weaker for NaI solutions than NaCl solutions, even for near-saturation concentrations. Although a_2 is small in comparison with a_1, the correction to γ, (2.7), that is made by retaining the a_2 term is up to 4% for NaI solutions. This maximum contribution was calculated assuming a density of $\bar{\rho} = 1.8\,\mathrm{g/cm^3}$ and using the corresponding index of refraction. For stratified solutions of NaI, the variation in γ due to z dependence is the dominant effect of the modifications to the Boussinesq synthetic schlieren formulation. Using $\bar{\rho} \in [0.99823, 1.8]\,\mathrm{g/cm^3}$, we may compare the resulting values of γ with a constant value given by $\gamma_0 = \frac{1}{g}\frac{\rho_0}{n_0}a_1$, where $\rho_0 = 0.99823\,\mathrm{g/cm^3}$ and $n_0 = \bar{n}(\rho_0)$. We obtain a total variation in γ of 56% of γ_0 by retaining the vertical dependence of $\bar{\rho}$ and $\bar{n}$ for a saturated NaI stratification. Density variations of $\sim 0.02\,\mathrm{g/cm^3}$ from the characteristic value ρ_0 produce variations in γ of approximately 1%. The results of the preceeding calculations depend only minimally on the value of

ρ_0.

Due to the typical practice of constructing solutions of known concentration rather than density, we also provide the functional relationship between these properties for NaI solutions. Assuming a quadratic dependence of the form

$$\bar{\rho}(c) = \rho_0 + b_1\, c + \frac{1}{2}\, b_2\, c^2, \tag{2.9}$$

where c is the solute concentration in g/ml and $\rho_0 = 0.99823\,\mathrm{g/cm^3}$, we find $b_1 = 0.7564 \pm 0.0001$ and $b_2 = -0.0348 \pm 0.0002$. Experimental data are shown with the fit curve in Figure 2.3(b). These new results allow for the quantitative measurement of non-Boussinesq fluid phenomena through the implementation of synthetic schlieren over a much larger range of ambient density variation than has been accessible previously.

Chapter 3

Wave Generation

3.1 Introduction

Section 3.2 contains a detailed description of the analysis methods that were used to obtain quantitative measurements of the wave frequencies, wavenumbers and amplitudes. The methods are specific to each quantity, but for all cases the process is based upon the analysis of time series images of the video recording for each experiment. Synthetic schlieren processing of the images, as described in Section 2.3, yields the wave field data that we focus upon in this chapter. The details of the analysis are followed in Section 3.3 by the experimental results for each of the fundamental wave properties. Wherever possible, these are compared with the predictions of the linear theory presented in Appendix A to illustrate the effects of the turbulent, large-amplitude generation mechanism upon each measured characteristic of the waves. In Section 3.3.4 we provide an estimate of the power of the primary beam, which requires a combination of the other quantities presented in this chapter.

3.2 Analysis Methods

For each experiment, vertical time series were made from the raw video footage at 24 equally spaced horizontal locations using the DigImage (Dalziel, 1992) software package. Further processing to obtain $N_t^2(z,t)$ was performed with a separate computer program. As shown in Figure 3.1(b), we reconstruct a spatial snapshot at any desired time from the set of vertical time series images. In this figure, vertical wavenumbers greater than 1.0 cm^{-1} have been filtered in the Fourier domain in order to remove small-scale spatial noise. Interpolation is also performed between grid points in the horizontal direction to smooth the image that results initially from the computational reconstruction of the snapshot. We calculate the envelope, $\langle N_t^2 \rangle$, as shown in 3.1(c), from $\sqrt{2}$ times the root mean square (rms) of 16 snapshots evenly spaced in time over one wave period (Sutherland and Linden, 2002) to obtain information about the average wave amplitude and beam structure in space and time. The direction of the increasing positive cross-beam coordinate, σ, is superimposed on the primary beam in (b) and (c). The orientation of the σ axis is calculated from the dispersion relation after the wave frequency has been determined as described in the next subsection.

3.2.1 Measurements of wave frequency

In the majority of cases, the wave frequencies were measured using time series of N_t^2 for $t \in [5T_c, 15T_c]$, where T_c is the oscillatory period of the cylinder. For several experiments with low forcing frequencies, the experimental data spans fewer than 15 periods, so the time window for frequency measurements was reduced. The standard time interval was chosen so that the waves were well-developed and reasonably steady. Figure 3.2 shows an example of the analysis process for one experiment in a NaI stratification with $R_c = 2.98\,\mathrm{cm}$, $A_c = 2.0\,\mathrm{cm}$, and $\omega_c = 1.53\,\mathrm{s}^{-1}$. As plotted in Figure 3.2(a), we constructed the horizontal time series of the data at a vertical distance of $5R_c$ above or below the equilibrium vertical position of the cylinder, depending on whether the cylinder was near the bottom or the top of the tank. The horizontal coordinate for the plot in (a) has been shifted such that the centre of the cylinder is located

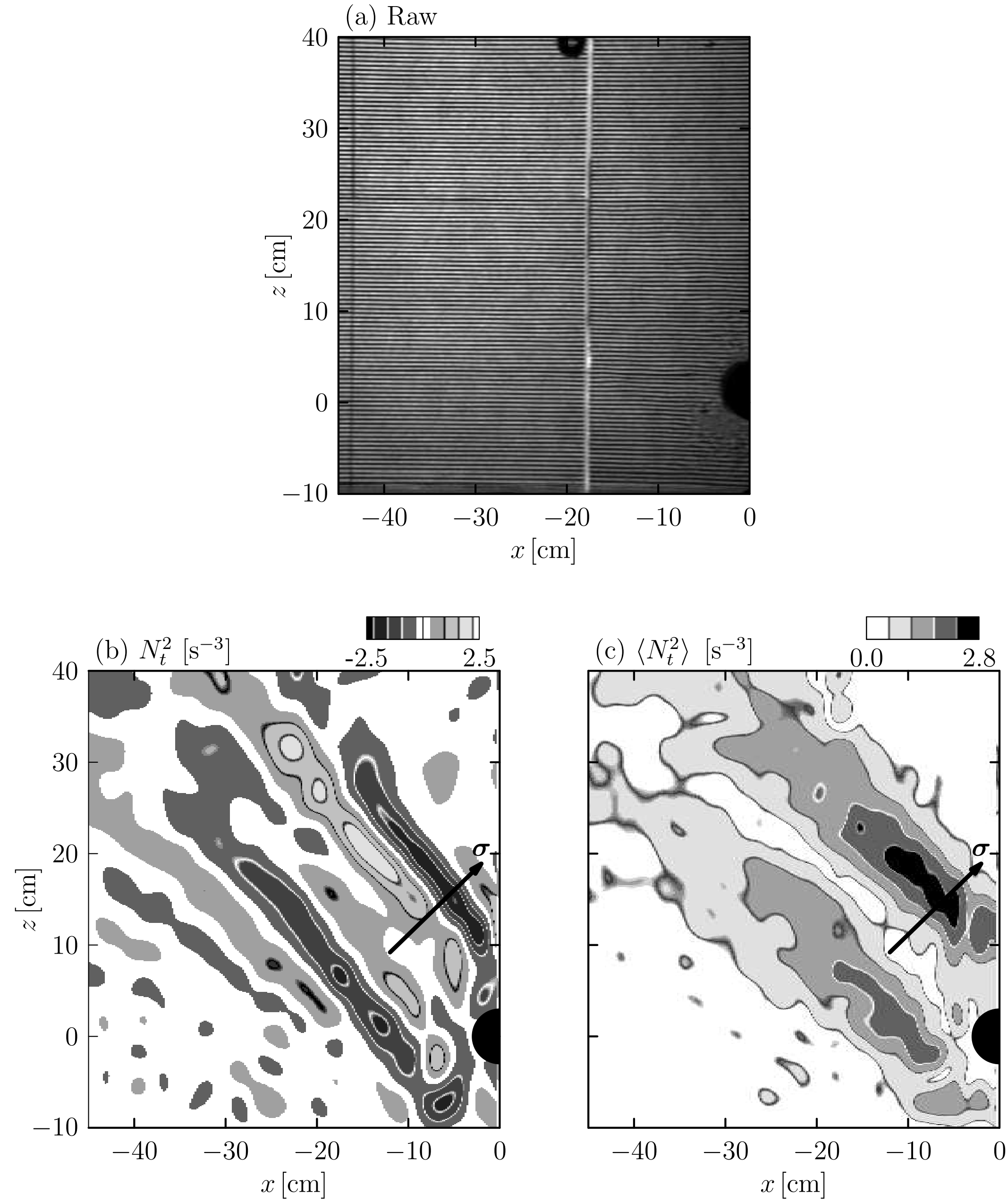

Figure 3.1: Synthetic schlieren is applied to yield the instantaneous value of N_t^2, plotted in (b) at a time corresponding to the raw image (a). The envelope $\langle N_t^2 \rangle$ over one wave period is shown in (c). In each case the coordinate origin is at the equilibrium position of the cylinder.

at $x = 0$. Eleven equally spaced profiles over the region $x \in [-6R_c, -5R_c]$, represented by the vertical lines in (a), were Fourier transformed in time to obtain power spectra in frequency space. The field for one representative profile is plotted in (b), with the corresponding spectrum shown in (c). The average of the 11 spectra was computed before finding the location of the peak in frequency, which we denote by ω_{igw}. For an improved measurement, we calculated ω_{igw} from a parabolic fit to the three discrete points that defined the peak of the power spectrum. The uncertainty, $\delta\omega_{\mathrm{igw}}$, in the measurement was taken to be the half-width of the parabolic curve that was centred about the peak. For the example shown in Figure 3.2(c), the wave frequency was equal to the cylinder frequency. However, in general the wave and cylinder frequencies need not be equal because of the turbulent generation process. A comparison between measured wave and cylinder frequencies is the topic of Section 3.3.1.

3.2.2 Measurements of wavenumber

Beginning with a snapshot of the N_t^2 field, the image was reflected about the horizontal coordinate of the center of the cylinder and rotated such that the lines of constant phase of the waves appeared horizontal. The clockwise angle of rotation is calculated as $\pi/2 - \Theta$, where Θ is the angle of the beam to the vertical direction, given by

$$\Theta = \cos^{-1}\left(\frac{\omega_{\mathrm{igw}}}{N_0}\right). \tag{3.1}$$

This is a consequence of the dispersion relation for internal waves. Through this processing of the image the horizontal and vertical axes correspond to the along-beam (r) and cross-beam (σ) coordinates respectively, as plotted in Figure 3.3(a) for a typical experiment. Note that the r axis as shown does not start from zero. For small values of the radial coordinate the schlieren pro-

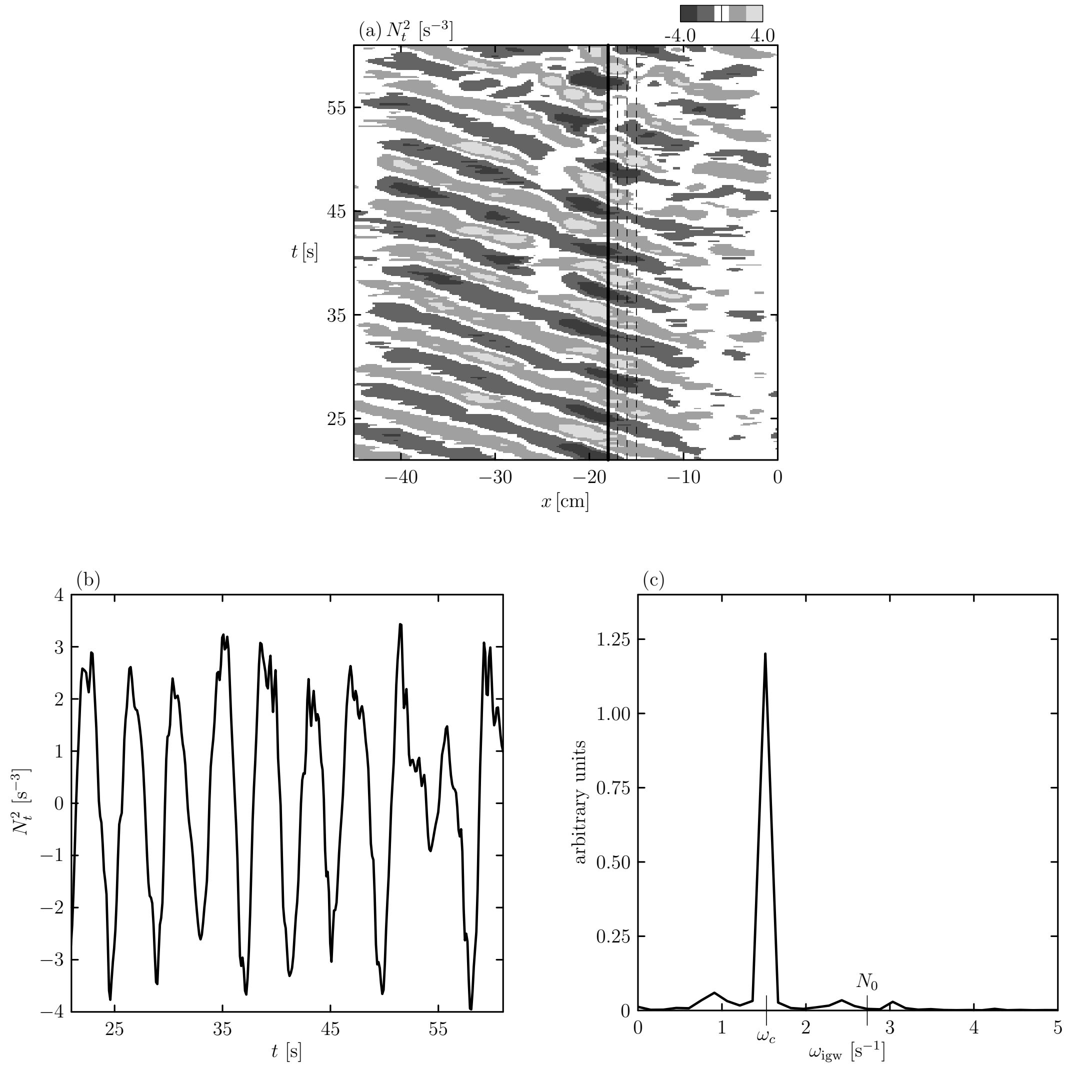

Figure 3.2: (a) A horizontal time series of the N_t^2 field is shown with vertical lines drawn schematically over the region of spatial averaging. A profile through the contour plot at the location of the solid dark line is shown in (b), with the corresponding power spectrum of the Fourier transform in time plotted in (c). The forcing and buoyancy frequencies are marked on the horizontal axis.

cessed data contains unreliable values due to the presence of the cylinder and the surrounding three-dimensional turbulence. We have restricted our analysis to $\sigma \geq 0$ because of potential interference between the primary beam and the reflected beam in the lower flank, for which $\sigma < 0$. Although interference is not predicted by theory, our experimental beams have more diffuse boundaries because of the turbulent generation process. The heavy dashed lines in Figure 3.3(a) correspond to the edges of the original schlieren image that has undergone reflection and rotation. The amplitude is not necessarily zero in the upper corners of (a), but the region for data acquisition did not include the areas outside of the dashed curves. In general, this restriction did not affect our analysis because we have focused on the primary beam and the amplitude of the signal was naturally decreasing to zero as the edge of the analysis window was approached. In some cases it was evident that a clockwise rotation by the angle $\pi/2 - \Theta$ resulted in beams that were not horizontal. Although we have been unable to determine the cause of this observation, in these cases a correction of up to ~ 0.1 rad was applied to yield nearly horizontal phase lines. Without this correction, it was obvious to the eye that a profile through the image at constant r would not be close to perpendicular to the phase lines of the beam. A spatially averaged profile, plotted as the solid curve in Figure 3.3(b), was computed from 11 evenly spaced profiles over $r \in [5R_c, 6R_c]$, which are represented by the dashed vertical lines in (a). The dashed curves in (b) are the envelope of the r-averaged N_t^2 profiles over one wave period, with the lower curve being the reflection of the positive amplitudes obtained from the rms. The profile shown at a particular phase moderately overshoots the envelope because the experimental signal includes noise and so is not perfectly sinusoidal in time. We then calculated the power spectrum, shown in (c), of the Fourier transformed data.

In all cases we observed a distribution of power over a range of wavenum-

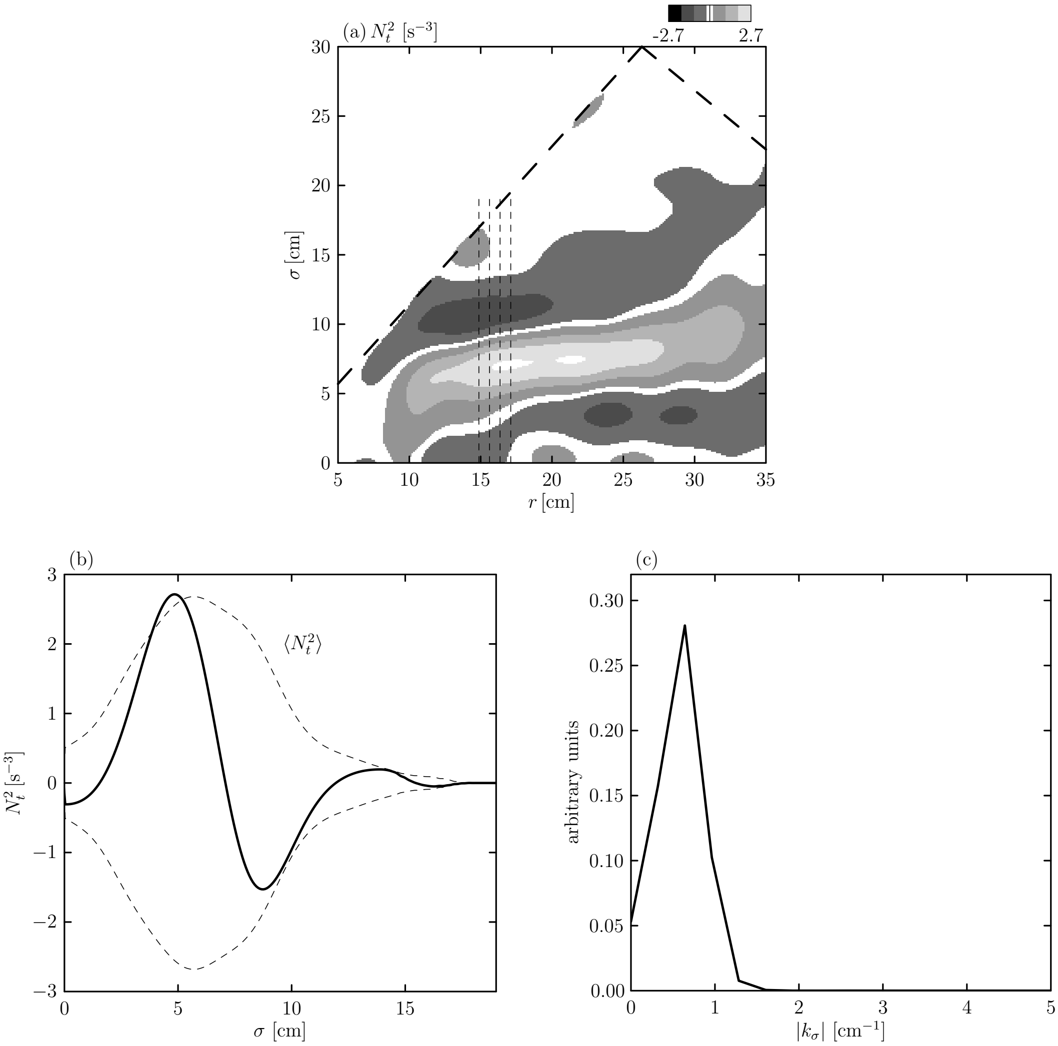

Figure 3.3: Contours of N_t^2 are shown in (a) after reflection and rotation about the position of the cylinder. The dashed line demarcates the regions in the upper corners of the image where no schlieren information is available. The r-averaged profile is given by the solid curve in (b), with the envelope, calculated as described in 3.2, given by the dashed curve. The power spectrum resulting from the Fourier transform of the solid curve is plotted in (c) as a function of cross-beam wavenumber.

bers, which is expected for a beam of internal waves. However, here we focus on the wavenumber with the maximum associated power in the Fourier spectrum, and denote its magnitude as k_σ^*. For each spectrum as shown in Figure 3.3(c), the peak value was found from a quadratic fit to the three points with the maximum amplitudes. The resulting peak values from 16 evenly spaced snapshots were then averaged in time for $t \in [4T_{\mathrm{igw}}, 5T_{\mathrm{igw}}]$. The wave period was calculated from the measured wave frequency as $T_{\mathrm{igw}} = 2\pi/\omega_{\mathrm{igw}}$. This interval in time was chosen because the beams were well-developed and significant distortions due to wave instabilities were not yet present. The uncertainty in the measurement of the cross-beam wavenumber, δk_σ^*, was taken to be the standard deviation determined from the averaging process. This procedure provides a characteristic value for an analysis of the wave lengthscale and is used in further calculations that involve the polarization relations.

3.2.3 Measurements of wave amplitude

For the analysis of wave amplitudes, we have focused on the N_t^2 field for times $t \in [4T_{\mathrm{igw}}, 5T_{\mathrm{igw}}]$ and the amplitude envelope was computed as described in Section 3.2. The processed images were reflected and rotated about the position of the cylinder, as described in the previous subsection. In order to capture the properties of the beam, we have computed a profile in the σ direction, averaged over a radial coordinate of $r \in [10\,\mathrm{cm}, 20\,\mathrm{cm}]$. Although we use the envelope, $\langle N_t^2 \rangle$, for this analysis, some "patchiness" is still evident in the final image that we use for further calculations. Averaging in the r-direction reduces some of the variability in the signal that is an artifact of processing rather than an indication of the wave structure. The lower bound of the spatial interval was chosen such that the measurements would be outside of the turbulent boundary layer around the cylinder. In general, this spatial range captured the region of maximum wave amplitude and also included sufficient areas of smaller amplitude so as not to over-estimate the characteristic value for the experiment. This characteristic amplitude, denoted by $A_{N_t^2}$, was taken as the maximum value extracted from the r-averaged profile, with its uncertainty given by the standard deviation.

3.3 Wave structure and transport

The results of the experimental analysis as described in Section 3.2 are presented in the same order in the following subsections.

3.3.1 Wave frequencies

In Figure 3.4 we compare the normalized wave frequencies, $\omega_{\mathrm{igw}}/N_0$, to the normalized forcing frequency, ω_c/N_0. In (a) the average power spectrum for each experiment is shown with an offset on the horizontal axis corresponding to the value of ω_c/N_0. For illustrative purposes, the spectra have been rescaled such that the maximum amplitude is the same for all experiments. The dashed line with a slope of 1 corresponds to the prediction of linear theory that the wave frequency is equal to the forcing frequency. In Figure 3.4(b) the value of ω_{igw} with peak power is plotted with a solid circle. The open circles correspond to secondary, lower amplitude peaks in the frequency spectrum. Two additional dashed lines with a slope of 2 and 3, respectively, are also shown in (b) to indicate frequency harmonics. For the experiments with the smallest relative forcing frequencies, the majority of the power in the frequency spectrum was at double the forcing frequency. When frequency-doubled waves were observed, a peak in the spectrum also occurred at the forcing frequency. For the lowest forcing frequency, another small-amplitude peak can be seen in the spectrum at three times the forcing value, but this is the only experiment that permits frequency tripling due to the upper limit of the buoyancy frequency. Also according to linear theory, no waves can be generated directly

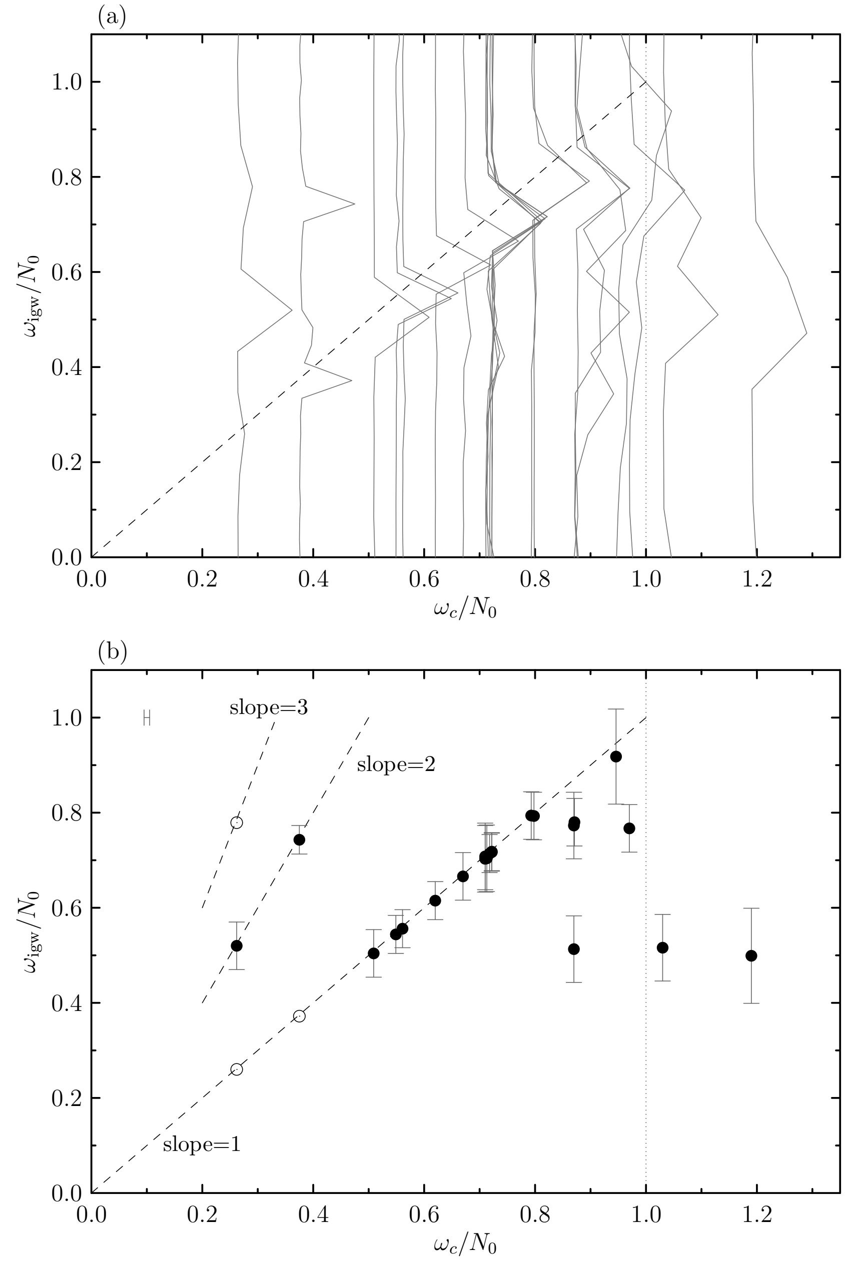

Figure 3.4: Measured frequency ω_{igw} versus cylinder frequency ω_c, both normalized by N_0. The dashed line with a slope of 1 corresponds to the prediction of linear theory, as described in the text. In (a), the power spectrum is shown for each experiment, with an offset on the horizontal axis that corresponds to the normalized forcing frequency. The frequency with the maximum power has been found and is plotted in (b) with solid circles. Open circles show the locations of secondary peaks in the spectra for the lowest frequency cases. A typical horizontal error bar is shown in the upper left-hand corner.

by the cylinder for ω_c above N_0, which is indicated on the plot by the dotted vertical line. Although the spectra are broader for forcing frequencies above the buoyancy frequency, we nonetheless observed propagating internal waves with $\omega_{\mathrm{igw}} \simeq 0.5N_0$ in these experiments due to generation by the oscillatory turbulent patch. The observed relative frequency corresponds to propagation at approximately 60° from the vertical. This result is near the largest angle of the ranges for turbulently generated waves found numerically by Taylor and Sarkar (2007) (35°– 60°) and experimentally by Dohan and Sutherland (2003) (42°– 55°).

Agreement with the theoretical prediction is closest for the range $\omega_c/N_0 \in [0.5, 0.8]$, where we see that the experimental data lie on the theoretical curve within the error bars in all cases. In the following sections, we focus on experiments in this frequency range because the waves exhibit the most coherent beam structure, thereby facilitating our analysis and interpretation of the data. For low forcing frequencies, frequency doubled and tripled wave beams are superimposed with waves having frequency $\omega_{\mathrm{igw}} \approx \omega_c$. This causes difficulties because the technique of rotating into (σ, r) coordinates for analysis becomes ambiguous. For supercritical forcing, the waves are generated purely by turbulence and the resulting structure is not a coherent beam. We observed a change in the qualities of the waves above $\omega_c/N_0 \simeq 0.8$, where the data turn off from the theoretically predicted curve.

3.3.2 Cross-beam wavelengths

In the linear regime the length scale of the waves is completely determined by the size of the cylinder (Hurley and Keady, 1997). In the current experiments, for which A_c is of the same order as R_c, we anticipate that the large-amplitude forcing may influence the wavenumber as well. In Figure 3.5(a) the inverse of the cross-beam wavenumber, $1/k_\sigma^*$, is plotted as a function of the cylinder radius. Due to the restriction of the frequency range as discussed in Section 3.3.1, only two different cylinder sizes remain in the final data set. From the plot it is evident that R_c is not an adequate predictor of the resulting wavenumber, particularly for the smaller values of oscillation frequency. Based on this separation of the data points according to frequency, we conclude that the frequency must be incorporated in order to find a relevant length scale.

Estimation of the Ozmidov length scale

Due to the turbulent nature of the wave generation process, we look for a length scale of turbulence that has physical relevance to the system. The Ozmidov length scale, L_O, is a measure of the scale in stratified turbulence at which buoyancy effects and inertial forces are equal (Kantha and Clayson, 2000). Thus it characterizes the maximum vertical extent of eddies in the flow. The Ozmidov scale is given in terms of the turbulent dissipation rate, ε, and the buoyancy frequency as (Thorpe, 2005)

$$L_O = \varepsilon^{1/2} N^{-3/2}. \tag{3.2}$$

We hypothesize that the size of the largest eddies in the turbulent patch surrounding the cylinder may influence the length scales of the resulting internal waves. Continuing with this physical intuition we estimate L_O for the experimental apparatus, as described in Section 2.2, by first finding an appropriate estimate of ε. We assume that the energy of the waves is small in comparison with the total energy input by the cylinder so that the turbulent dissipation rate may be approximated by the rate of energy input per unit mass. The validity of this assumption is discussed in Section 3.3.4 in the context of measurements of the wave power.

From observations of the unprocessed experimental data, we find that when the cylinder oscillates, fluid in the bounding region above or below the cylinder

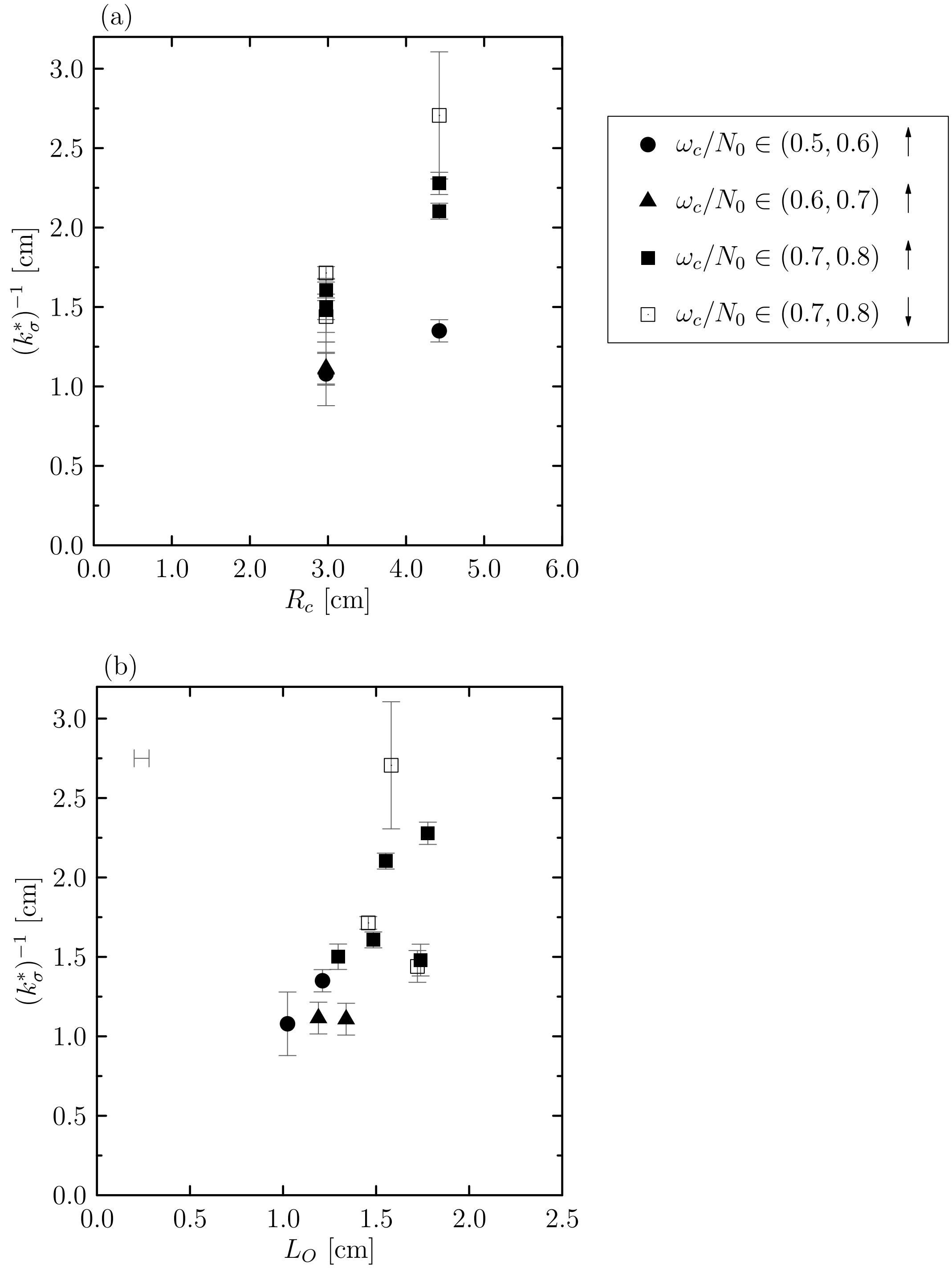

Figure 3.5: The inverse of the cross-beam wavenumber as a function of (a) R_c and (b) the Ozmidov scale, L_O. A typical horizontal error bar is shown in the upper left-hand corner of (b). In the legend, the direction of the arrows corresponds to the direction of propagation of the primary beam (measurements of upward- or downward-propagating waves). Symbols are designated according to the relative forcing frequency for each experiment.

is displaced and flows around the cylinder to the opposite side. This appears to be the primary process occurring in the generation of the turbulent patch, and it is also consistent with our qualitative observation that in quasi-steady state the oscillatory turbulence is out of phase with the cylinder. The time lag is produced as the fluid from below the cylinder flows around the cylinder toward the top, or vice versa. We will use this process as a model from which to estimate the relevant velocity and time scales for the input of kinetic energy by the oscillations of the cylinder. Here it should be emphasized that we are performing an estimate with the aim of obtaining the correct form of the dependence on the experimental parameters.

First we calculate the area, $\mathcal{A}$, in the (x, z) plane of the fluid that is displaced by the downward motion of the cylinder with amplitude A_c. We obtain

$$\mathcal{A} = A_c R_c \sqrt{1 - \frac{A_c^2}{4R_c^2}} + R_c^2 \left[\pi - 2\sin^{-1}\left(\sqrt{1 - \frac{A_c^2}{4R_c^2}} \right) \right], \tag{3.3}$$

which is dominated by the first term. Assuming that $A_c \lesssim R_c$, which is the case for our experiments, this expression may be treated reasonably as $\mathcal{A} \sim A_c R_c$. Thus, the mass of fluid per unit length along the cylinder that is displaced is roughly $\rho_0 A_c R_c$, where ρ_0 is a characteristic density at the position of the cylinder. To estimate the velocity of the displaced fluid we assume that it travels a vertical distance of $2R_c$ in a timescale of ω_c^{-1}, yielding a characteristic speed of $v \sim 2\,\omega_c R_c$. From these calculations we find that the rate of kinetic energy input per unit length for the displaced fluid is approximately $\rho_0 (A_c R_c)(2\omega_c R_c)^2 \omega_c$, where the third power of ω_c is a result of finding the quantity per unit time. To obtain the input rate of energy per unit mass, we divide this quantity by the fluid density and the area of the region of energy input, which to leading order is πR_c^2. Thus our final estimate of ε becomes

$$\varepsilon \sim \frac{(A_c R_c)(2\,\omega_c R_c)^2 \omega_c}{\pi R_c^2} \sim A_c R_c\, \omega_c^3. \tag{3.4}$$

From (3.2) the resulting expression for L_O is then

$$L_O \sim \sqrt{A_c R_c}\left(\frac{\omega_c}{N}\right)^{3/2}. \tag{3.5}$$

Typical values of L_O for our experimental parameters are on the order of 1 cm, which indeed is the characteristic scale of the turbulent patch observed above and below the cylinder.

In Figure 3.5(b) $(k_\sigma^*)^{-1}$ is plotted as a function of our estimated L_O. There are several encouraging features of this plot in comparison with that shown in (a). Due to the introduction of the frequency to the lengthscale on the horizontal axis, the experiments with lower forcing frequencies are no longer separated from the higher frequency cases. We do not expect perfect collapse of the data because of the significant level of noise present in the experimental data. However, Figure 3.5 demonstrates that a clearer trend emerges through a comparison between the wave lengthscale and a lengthscale of stratified turbulence. Although we acknowledge that the values of the Ozmidov scale are an estimate, the relationship between $(k_\sigma^*)^{-1}$ and L_O is of order 1, which makes a direct correspondence between these quantities more physically plausible. Some of the scatter in the data may be attributed to our treatment of the beam as monochromatic in space. Since we have retained only the peak wavenumber in our analysis, the results for each experiment may be affected differently by this simplification depending on the true distribution of power with wavenumber. The result that the lengthscale of the waves appears to be determined by a lengthscale of turbulence reinforces our interpretation of the wave generation process as turbulent.

3.3.3 Wave amplitudes

Although we measured the amplitude $A_{N_t^2}$ directly, we may use the Boussinesq polarization relations as summarized in Table 3.1 to find the amplitude of the vertical displacement of the waves, given by

$$A_\xi = \frac{A_{N_t^2}}{N_0^3 k_x \sin\Theta} = \frac{A_{N_t^2}}{N_0^3 k_\sigma^* \cos\Theta \sin\Theta}. \tag{3.6}$$

We normalize A_ξ by the horizontal wavelength, $\lambda_x = 2\pi/k_x$, to provide a more physically meaningful interpretation of the data. The final values were calculated as

$$\frac{A_\xi}{\lambda_x} = \frac{A_{N_t^2}}{2\pi N_0^3 \sin\Theta}. \tag{3.7}$$

We have plotted the normalized amplitude as a function of A_c/L_O because of the result presented in Section 3.3.2 that L_O, rather than R_c, determines the length scale of the waves. As shown in Figure 3.6, there is a clear separation in the ratio A_ξ/λ_x for NaCl and NaI experiments, with an approximately constant ratio of $\sim$ 2.5% for all NaI experiments. In previous work (Dohan and Sutherland, 2003; Aguilar and Sutherland, 2006) with NaCl stratifications it was observed across experiments that A_ξ/λ_x collapses to a value in the range of 2-4%, regardless of the forcing amplitude. We do not have an explanation for the observed increase in the ratio for NaCl experiments. The effect of the smaller buoyancy frequency for NaCl stratifications is magnified by the cubic power of N_0 in (3.6). However, there is no obvious physical reason to anticipate that this difference between the amplitude ratios should be based on stratification alone.

For all calculations in the analysis of the wave generation, we have assumed that the fluid can be treated as Boussinesq, because the extent of vertical propagation is small in comparison with the density scale height. As shown in Figure 3.6, the vertical error bars are sufficiently large as to produce a region of overlap between the data for upward- and downward-propagating waves. If trends in the data are significant, the slightly reduced amplitudes for downward-propagating cases may indicate that the region of observation is

Field variable, b	Complex amplitude, A_b
ξ	A_ξ
$w = \frac{\partial \xi}{\partial t}$	$A_w = -i\omega A_\xi$
$\frac{\partial \psi}{\partial x} = w$	$A_\psi = -\frac{\omega}{k_x} A_\xi$
$u = -\frac{\partial \psi}{\partial z}$	$A_u = i\omega \frac{k_z}{k_x} A_\xi$
$\rho = -\frac{d\bar{\rho}}{dz}\xi$	$A_\rho = \frac{\rho_0}{g} N^2 A_\xi$
$\frac{\partial p}{\partial x} = -\rho_0 \frac{\partial u}{\partial t}$	$A_p = i\omega^2 \rho_0 \frac{k_z}{k_x^2} A_\xi$
$\Delta N^2 = -\frac{g}{\rho_0}\frac{\partial \rho}{\partial z}$	$A_{\Delta N^2} = -ik_z N^2 A_\xi$
$N_t^2 = \frac{\partial}{\partial t}(\Delta N^2)$	$A_{N_t^2} = k_z \omega N^2 A_\xi$

Table 3.1: Polarization relations for two-dimensional, small-amplitude waves in an inviscid, uniformly stratified Boussinesq fluid. The complex amplitude, A_b, of the velocity components (u, w), streamfunction (ψ), density perturbation (ρ), pressure (p), change in buoyancy frequency (ΔN^2) and its time derivative (N_t^2) is given in terms of the vertical displacement amplitude, A_ξ. The horizontal and vertical wavenumbers are related through $\tan\Theta = k_z/k_x$.

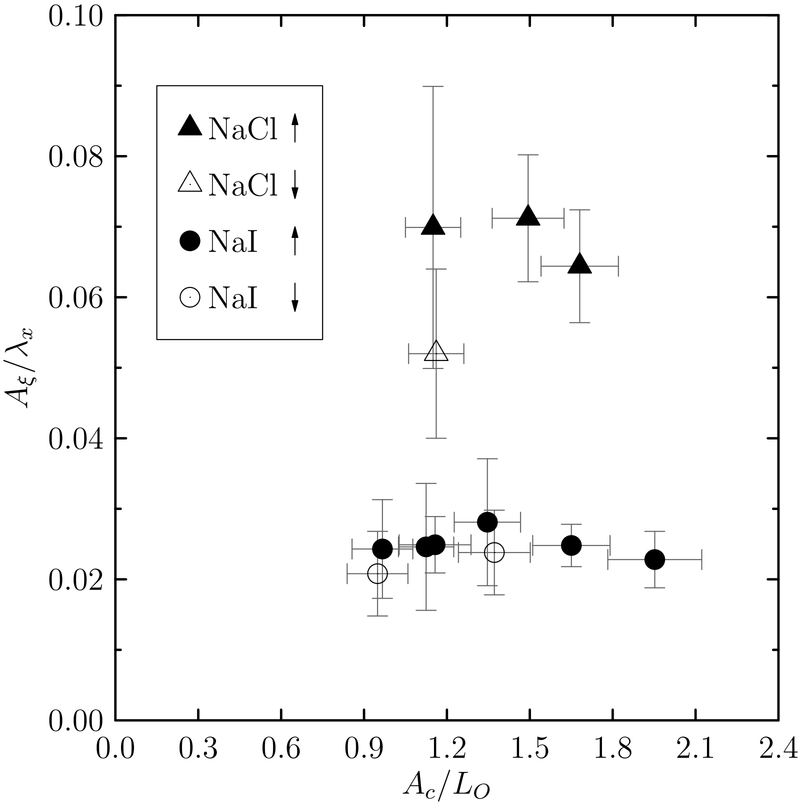

Figure 3.6: Vertical displacement amplitude, A_ξ, normalized by horizontal wavelength, λ_x, shown as a function of normalized cylinder amplitude. Upward(downward)-pointing arrows denote measurements of upward(downward)-propagating waves.

at the threshold of non-Boussinesq asymmetry between the directions of vertical propagation. However, we cannot conclude that the data shown contains evidence of non-Boussinesq wave behaviour.

3.3.4 Wave power

We use the measurements of the characteristic wavenumber and amplitude, as described in the previous subsections, to calculate the average energy flux of the primary beam, from which we compute the wave power. The present analysis is restricted to experiments for which $\delta k_\sigma^*/k_\sigma^* \leq 0.1$ and $\delta A_{N_t^2}/A_{N_t^2} < 0.2$ simultaneously. Although these are significant fractional uncertainties, for the calculation of wave power we wish to retain the experiments for which the characteristic values are as unambiguous as possible.

From the polarization relations shown in Table 3.1 we obtain the following expression for the time-averaged vertical energy flux of a monochromatic plane wave with wavenumber k_σ:

$$\langle F_E \rangle = \langle wp \rangle = \frac{1}{2}\rho_0 \frac{A_{N_t^2}^2}{N_0^3 \cos\Theta \sin\Theta k_\sigma^3}. \tag{3.8}$$

The use of this expression in our analysis requires that modes other than k_σ do not contribute significantly to the N_t^2 field. However, based on the characteristics of the experimental power spectra, it is unreasonable to expect an accurate result for power if the beam is treated as monochromatic. Therefore, we have modified the above expression to account for the contributions from all cross-beam modes, k_n, with non-negligible power. When referring to the Fourier spectrum, we use the term “power” to refer to the squared magnitude of the Fourier coefficient of a particular mode of the N_t^2 signal, and denote it by $\mathcal{P}_n(k_n)$. We replace the amplitude and characteristic wavenumber with a sum over modes, i.e.

$$\langle F_E \rangle = \frac{1}{2}\rho_0 \frac{1}{N_0^3 \cos\Theta \sin\Theta} \sum_n \frac{A_n^2}{k_n^3}. \tag{3.9}$$

The images used in the present analysis were processed using the same procedure as for the wavenumber analysis, as described in Section 3.2.2. Signal attenuation with increasing σ and a geometric effect caused by the rotation of the processed images resulted in a region of zero amplitude for the largest values of σ. Based on the properties of the FFT algorithm that we have employed, we account for this in our analysis by scaling the amplitude of a mode according to the ratio L_σ/L, where L_σ is a measure of the beam width and L is the length of the spatial domain for the Fourier transform. In this case the amplitude, A_n, that one would obtain from the transform is related to the amplitude of the real signal, A, through

$$A_n = \left(\frac{L_\sigma}{L}\right) A. \tag{3.10}$$

We find that the squared amplitude is given in terms of the power by

$$A_n^2 = \left(\frac{2}{L_\sigma/L}\right)^2 P_n. \tag{3.11}$$

To obtain the total power of the primary beam, we multiply the vertical energy flux by the area of a horizontal cross-section through the beam, $L_c L_x = L_c L_\sigma/\cos\Theta$, in which L_c is the length of the cylinder. Through this step and the substitution of (3.11) into (3.9) we arrive at the expression for the total measured power of the experimental beam:

$$P_{\text{expt}} = \frac{2\rho_0 L_c L^2}{N_0^3 \cos^2\Theta \sin\Theta L_\sigma} \sum_n \frac{\mathcal{P}_n}{k_n^3}. \tag{3.12}$$

In order to use the above expression we also require a quantitative method of determining the beam width, L_σ. We express L_σ in terms of a characteristic wavelength, λ^*, and an undetermined parameter, α, as

$$L_\sigma = \alpha\lambda^* = \frac{2\pi\alpha}{k_\sigma^*}. \tag{3.13}$$

By substituting this expression into (3.10) with $A_n \to A_*$ corresponding to the amplitude of the waves with $k_n \to k_\sigma^*$, we obtain

$$\alpha = \frac{A_*}{A}\left(\frac{k_\sigma^* L}{\pi}\right) = \frac{1}{\alpha}\frac{\mathcal{P}_*^{1/2}}{A}\left(\frac{k_\sigma^* L}{\pi}\right)^2, \tag{3.14}$$

then rearranging for α, we find

$$\alpha = \frac{\mathcal{P}_*^{1/4}}{A^{1/2}}\left(\frac{k_\sigma^* L}{\pi}\right). \tag{3.15}$$

For our estimate of α, we take the power of the mode for which k_n is closest to k_σ^*, and we use the characteristic amplitude, $A_{N_t^2}$, as described in Section 3.2.3. This yields values of $\alpha \in [1.6, 2.2]$ across all experiments. Comparison with the structure of the original N_t^2 profiles in the σ direction shows that this range of α is reasonable when we consider that it characterizes the number of wavelengths contained in the primary beam.

For a theoretical prediction of the time-averaged power radiated by a single wave beam, we refer to the linear, inviscid solution of Hurley (1997). Although the absence of viscosity is a further simplification in comparison with experiments, viscous attenuation should not play a large role over the moderate distance from the cylinder at which we focus our observations. Note that we do not expect the analytic expression to capture accurately the power radiated by a beam in the experiments because of energy loss to the turbulent boundary layer. However, we provide the theoretical background as a reference point for the expected behaviour of an idealized system. Ignoring viscosity, for the beam in the first quadrant the spatial dependence of the streamfunction, $\Psi(r, \sigma)$, is given by

$$\Psi = \begin{cases} \frac{1}{2} W R_c e^{-i\Theta}\left[-\frac{\sigma}{R_c} - i\sqrt{1-(\sigma/R_c)^2}\right], & |\sigma/R_c| < 1 \\ 0, & |\sigma/R_c| > 1 \end{cases}, \tag{3.16}$$

where W is the maximum of the magnitude of the cylinder velocity. The corresponding along-beam velocity is $u_r = \frac{\partial\psi}{\partial\sigma}$, where $\psi = \Psi\exp(-i\omega_c t)$. An integral of the average radial energy flux, $\langle u_r p \rangle$, where p is the pressure field, is computed over the region bounded by the tangents to the cylinder to obtain the power. From the linearized Boussinesq equations we obtain

$$p = -(i\omega_c \rho_0 \tan\Theta)\psi, \tag{3.17}$$

where ρ_0 is a characteristic density. Thus, using $u_r = \partial\psi/\partial\sigma$, for the average power P we have

$$P = \int_{-R_c}^{R_c} \langle u_r p \rangle \, d\sigma = \frac{\pi}{8}\rho_0 W^2 \omega_c R_c^2 \tan\Theta. \tag{3.18}$$

For comparison with the experimental results we have computed the time average of the power of the primary beam using (3.18). Denoting this as P_{thy} and recasting the result in terms of our experimental parameters, we obtain

$$P_{\text{thy}} = \frac{\pi}{8}\rho_0 \left(\frac{N_0^2}{\omega_{\text{igw}}^2} - 1\right)^{1/2} \omega_{\text{igw}} R_c^2 (A_c\,\omega_c)^2 L_c. \tag{3.19}$$

Here ω_{igw} is the internal wave frequency, which in general may differ from ω_c for our experiments. The use of both ω_{igw} and ω_c in the calculation of P_{thy} arises from the conversion of parameters in (3.18) to the variables in our notation. The product of $A_c\omega_c$ is the magnitude of the maximum velocity of the oscillating cylinder, whereas the single power of ω_{igw} is a result of our distinction between the properties of the waves and the cylinder. In the analytic formulation it is unnecessary to introduce a separate wave frequency. For the experiments that we are analyzing here, ω_{igw} differs very little from ω_c because we have restricted our focus to a particular range of forcing frequencies, as discussed in Section 3.3.1. We have expressed P_{thy} in terms of the wave frequency rather than the angle from the vertical because for some experiments there is a discrepancy between the predicted and observed angles. A formulation in terms of the frequency, which in the analytic problem would be equivalent to an expression using the propagation angle, allows us

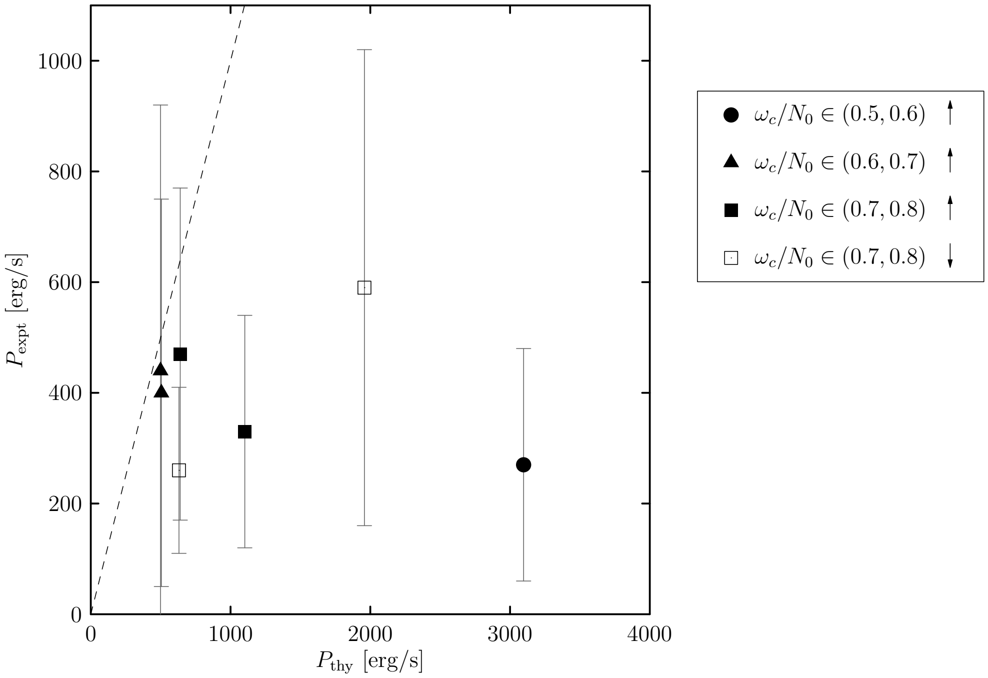

Figure 3.7: Experimentally measured power versus theoretically predicted power of the primary beam. 1 erg = 1 $\mathrm{g\,cm^2\,s^{-2}}$.

to use measured values rather than the less precisely obtained wave angle. For calculations of both P_{expt} and P_{thy} we have used characteristic densities of $\rho_0 = 1.25\,\mathrm{g/cm^3}$ for NaI stratifications and $\rho_0 = 1.1\,\mathrm{g/cm^3}$ for NaCl stratifications. These values were estimated from the experimental measurements of the density at the vertical level of our analysis of wavenumber and amplitude. We do not expect agreement between the experimentally measured power and the value predicted by (3.18) because the analytic result was derived under the assumptions of linear, Boussinesq theory. Although we did not observe significant deviations from Boussinesq conditions for the location of the current measurements, i.e. upward- and downward-propagating waves are quantitatively similar, the small-amplitude assumption does not hold. We pursue the comparison between P_{expt} and P_{thy} in an attempt to gain insight into the effects of the large-amplitude forcing on the resulting energy transport of the waves.

Figure 3.7 shows a plot of the experimentally measured power versus the theoretical prediction. (Note that the horizontal and vertical scales differ significantly.) The large vertical error bars on the data points are a result of adding significant contributions from several of the variables in (3.12). Namely, the largest contributions to the final error were due to the uncertainties in Θ, L_σ, and P_n, the last of which was estimated from the standard deviation of the time-averaged power spectrum. The experimental measurements and theoretical predictions are similar for small values of P_{thy}, but the two values deviate more with increasing forcing intensity. In general, we expect the experimental values to be less than the theoretically predicted power, because the coupling of the cylinder to the internal waves is affected by the development of the turbulent boundary layer. Where the theory predicts an increasing rate of energy transport by waves, we hypothesize that much of the forcing energy is lost to turbulent kinetic energy in the bounding region of the cylinder. Here we may use the expression for ε, (3.4), to estimate the total turbulent dissipation rate. The product of $\rho_0\varepsilon$ with the characteristic volume of displaced fluid, $\sim A_cR_cL_c$, yields an approximate dissipation rate of $\rho_0(A_cR_c)^2L_c\omega_c^3$. Using characteristic experimental values, we obtain an estimate of moderately larger than 2000 erg/s. Therefore, it is unsurprising that we observe smaller wave powers than predicted by theory. In particular, the estimated dissipation rate is comparable to the discrepancy between the values of P_{thy} and P_{expt} as the forcing intensity is increased. Our assumption that the energy dissipation rate ε is approximately equal to the rate of energy input, which neglects loss due to waves, is reasonable considering the relatively small magnitude of the measured wave power compared with the estimated rate of energy input.

Chapter 4

Instabilities and Breaking

4.1 Introduction

As discussed in Section 3.3.3, we did not observe non-Boussinesq growth of the wave amplitudes for upward-propagating beams through the use of synthetic schlieren. Although we cannot attribute the breakdown of the wave beams to the strong background stratification, the occurrence of instabilities remains an observation that requires further investigation. The fully three-dimensional flow that develops as the waves break down into turbulence eliminates quantitative synthetic schlieren as a tool for measurement or visualization of the process. Therefore, in this chapter we describe two other techniques through which we obtain information about the wave breakdown. Section 4.2 contains details about the use of conductivity probe measurements at fixed spatial locations to obtain the corresponding vertical displacement field. We explain a systematic technique for the qualitative analysis of wave breakdown from synthetic schlieren images in Section 4.3.1, followed by the results in Section 4.3.2. The findings of this qualitative analysis guide our hypothesis about a candidate instability mechanism through which the beams break down. For an investigation of the instability we have performed numerical simulations using a fully nonlinear code. A brief description of the code and an order-of-magnitude comparison between the results of the simulations and experiments are given in Section 4.4.1.

4.2 In-situ probe measurements

Synthetic schlieren provides a means of measuring quantitatively the structure and amplitude of internal waves in space and time. In the previous sections we have demonstrated the application of synthetic schlieren to experiments in strongly stratified fluids. We have used a separate quantitative technique for one characteristic experiment, in which measurements were made of the waves at a fixed location as they evolved in time. This provides an independent means through which we may observe the establishment of the wave field and its subsequent breakdown into turbulence.

A conductivity probe was used to perform a vertical traverse of the background stratification in the spatial region of interest, with approximately 42 measurements of voltage, V, per vertical centimeter. The probe was then placed at fixed locations in space for a series of three experiments in which a cylinder with $R_c = 4.43\,\mathrm{cm}$ and $A_c = 2.0\,\mathrm{cm}$ was oscillating with frequency $\omega_c = 1.96\,\mathrm{s}^{-1}$ approximately 10 cm above the bottom of the tank. The probe provided measurements of the voltage with a resolution in time of $\Delta t = 0.05\,\mathrm{s}$. The horizontal location of the probe was approximately 30 cm from the center of the cylinder while the vertical coordinate was set at $z = 45$, 40, and 35 cm successively above the bottom of the tank. In all cases the total depth of the fluid was $H_t \simeq 55\,\mathrm{cm}$.

The time series measurements of voltage were translated into densities using the function $\bar{\rho}(V)$ obtained from a linear fit to four discrete measurements of voltage for densities in the range of $[0.998, 1.30]\,\mathrm{g/cm}^3$. With waves in the fluid, the perturbation density at each vertical level was computed by subtracting the background density that was measured prior to the start of the cylinder oscillations. The wave vertical displacement, ξ, was then calculated according to

$$\rho = -\frac{d\bar{\rho}}{dz}\xi, \tag{4.1}$$

where ρ is the perturbation density and the background density gradient at each of the three vertical levels was found through

$$\frac{d\bar{\rho}}{dz} = \frac{dV}{dt}\frac{d\bar{\rho}}{dV}\frac{dt}{dz}. \tag{4.2}$$

Time series of the vertical displacement are shown in Figure 4.1 for each vertical level. The motor driving the oscillations of the cylinder was turned on at $t = 30\,\mathrm{s}$ for (a) and $t = 20\,\mathrm{s}$ for (b) and (c), and was turned off at $t \simeq 150\,\mathrm{s}$ for each experiment. In all cases, we observe at first a regular, periodic signal in time, with growth in amplitude as the initial transient reaches and passes the location of the probe. Based on the background stratification and the forcing frequency, we expect close agreement between the cylinder and wave frequencies because $\omega_c/N_0 \in [0.5, 0.8]$, as discussed in Section 3.3.1. A closer examination of the early times in Figure 4.1 yields a wave period that is similar to the cylinder period of $T_c = 2\pi/\omega_c = 3.2\,\mathrm{s}$. For each plot the vertical axis is the same to allow for direct comparison of the wave amplitudes at varying location in the vertical. The schlieren measurements as reported upon in Section 3.3.3 yielded an estimate of the amplitude of the waves for $t \in [4T_{\mathrm{igw}}, 5T_{\mathrm{igw}}]$ from an average over $r \in [10\,\mathrm{cm}, 20\,\mathrm{cm}]$. For an experiment with the same forcing parameters as the experiment shown here, the estimated vertical displacement amplitude was $A_\xi = 0.5\,\mathrm{cm}$. Although the spatial locations of the measurements differed, the conditions should be the most similar to those at $z = 35\,\mathrm{cm}$ in the present analysis. The appropriate time for comparison of the wave amplitudes is approximately 4 wave periods after the oscillations of the cylinder began, which is $t \simeq 33$ s. While we do not expect exact agreement between the measurements because of the

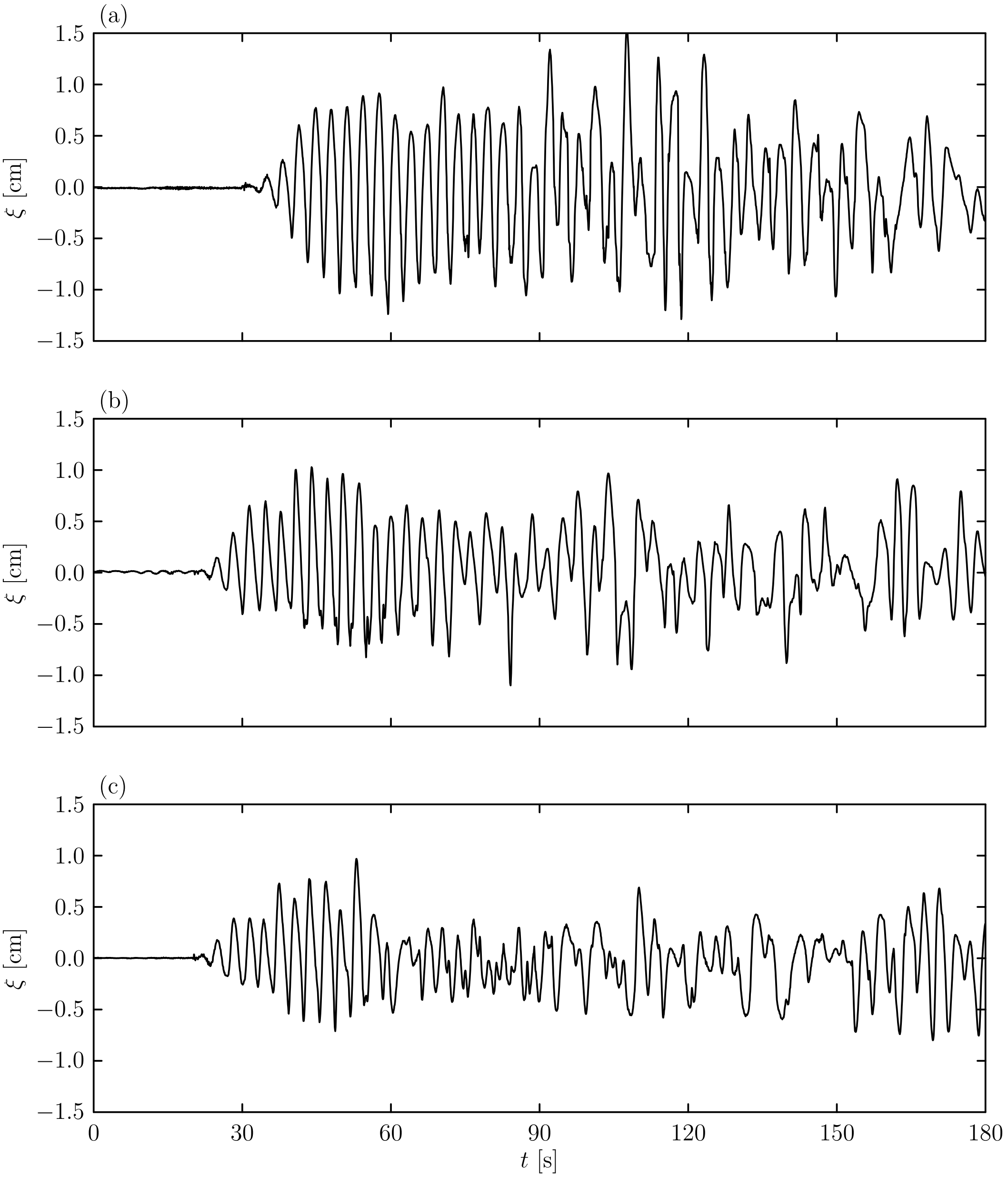

Figure 4.1: Time series of the vertical displacement measured at $z = 45, 40, 35\,\mathrm{cm}$ in (a), (b), and (c) respectively, with the same cylinder and forcing parameters in each case.

different techniques of instantaneous measurement and averaging over space and time, the magnitude of the wave vertical displacement is within approximately 25% of the value of 0.5 cm obtained using synthetic schlieren. As shown in Figure 4.1, after a finite time the signal becomes irregular and the wave amplitude varies erratically. We consider this change in the regularity of the signal the signature of turbulence onset. The occurrence of large wave amplitudes or irregularity in the time series correlates well with the observation of significant distortions in the schlieren image of horizontal lines behind the tank, as described in Section 4.3.1.

4.3 Wave breakdown: qualitative observations

4.3.1 Method

In order to gain insight into the mechanism for the observed instabilities, a qualitative examination was performed of the raw video footage for a subset of experiments. The collection of experiments included both NaCl and NaI stratifications, as well as the full range of cylinder radius, amplitude, and oscillation frequency. A consistent, although qualitative, criterion was chosen to mark the onset of significant disturbances to the beam structure; we will refer to this phenomenon as wave breakdown. The horizontal black and white lines of the schlieren image were monitored visually for the first occurrence of the lines appearing to be oriented vertically at a location outside of the turbulent region bounding the cylinder. An example of the visual characteristics of the schlieren image is shown in Figure 4.2. The experiment and spatial region are the same for each frame, with time increasing from (a) to (c). A typical image resulting from a coherent wave beam is shown in (a), which includes visible deflections of the lines from their undisturbed orientation. The region is shown in (b) 4 seconds later with clear qualitative changes occurring in the im-

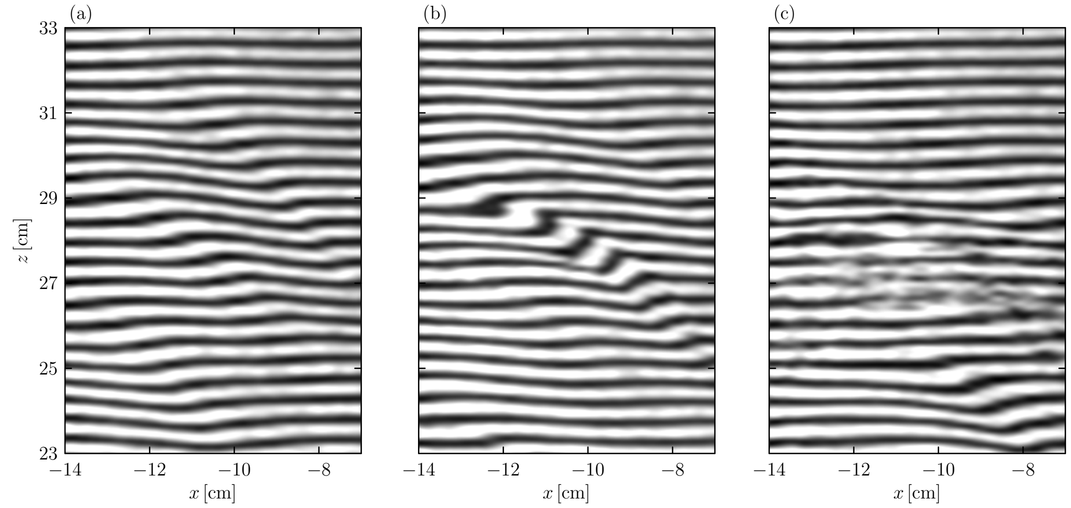

Figure 4.2: Close-up view of synthetic schlieren background showing evolution of image characteristics. (a) Typical distortions of the image due to waves. (b) The image when satisfying the criterion for breakdown. (c) Loss of resolution of the lines. $(x, z) = (0, 0)$ corresponds to the equilibrium position of the cylinder.

age. Our criterion for wave breakdown is satisfied at $(x, z) \simeq (-11\,\mathrm{cm}, 28\,\mathrm{cm})$, where the lines become vertical and appear to be "overturning." The image in (c), taken 7 seconds after the time of (b), shows blurring and the inability of the camera to resolve each separate line due to the development of fully three-dimensional turbulence. We interpret this evolution of the raw image as evidence of the evolution of the beam instability, but these features alone do not provide significant insight into the instability mechanism. We provide a discussion of potential causes for wave breakdown in Section 4.3.2.

For each experiment, several frames separated by 1 second were made from the video recording, starting at approximately the time of breakdown. From these still images the initial breakdown could be examined more easily and precisely. In each case, this technique was used to estimate the time and location at which breakdown occurred, which can then be compared for different forcing parameters of the cylinder. We emphasize that this analysis focuses on the first occurrence of the image "overturning," as shown in Figure 4.2(b).

Such overturning often is subsequently observed at different locations in the tank for later times in the experiment.

4.3.2 Results of qualitative synthetic schlieren analysis

The qualitative data, obtained from unprocessed schlieren images as described in Section 4.3.1, yielded several significant results. For some experiments, the breakdown criterion was not satisfied at any time that the cylinder was oscillating. It was common to these experiments that the forcing frequency was very near to or above the background buoyancy frequency, or the amplitude of oscillation was the smallest of our parameter range. This result for high frequency forcing is consistent with the quantitative synthetic schlieren measurements, in which the wave signal was weaker and less coherent than for mid-range forcing frequencies. Thus, we should not necessarily expect significant growth and transition to instability for the waves generated by high frequency forcing. The occurrence of wave breakdown in both upward- and downward-propagating experiments confirms that non-Boussinesq growth of upward-propagating waves is not responsible for the behaviour. Another trend in the observations is that the time of wave breakdown varies significantly across experiments. For the same cylinder radius and amplitude, a change in the forcing frequency yielded an opposite change in the observed time of breakdown, i.e. a decrease (increase) in frequency resulted in a later (earlier) breakdown. This is a physically reasonable consequence of the change in the timescale of wave beam development due to the change in frequency. The effects of cylinder radius and amplitude on the breakdown time and location appear to be dominated by the forcing frequency in this qualitative analysis.

There are several possible scenarios, which are represented schematically in Figure 4.3, that could lead to the breakdown of waves as observed. We expect that nonlinear effects are the most significant in regions of beam self-

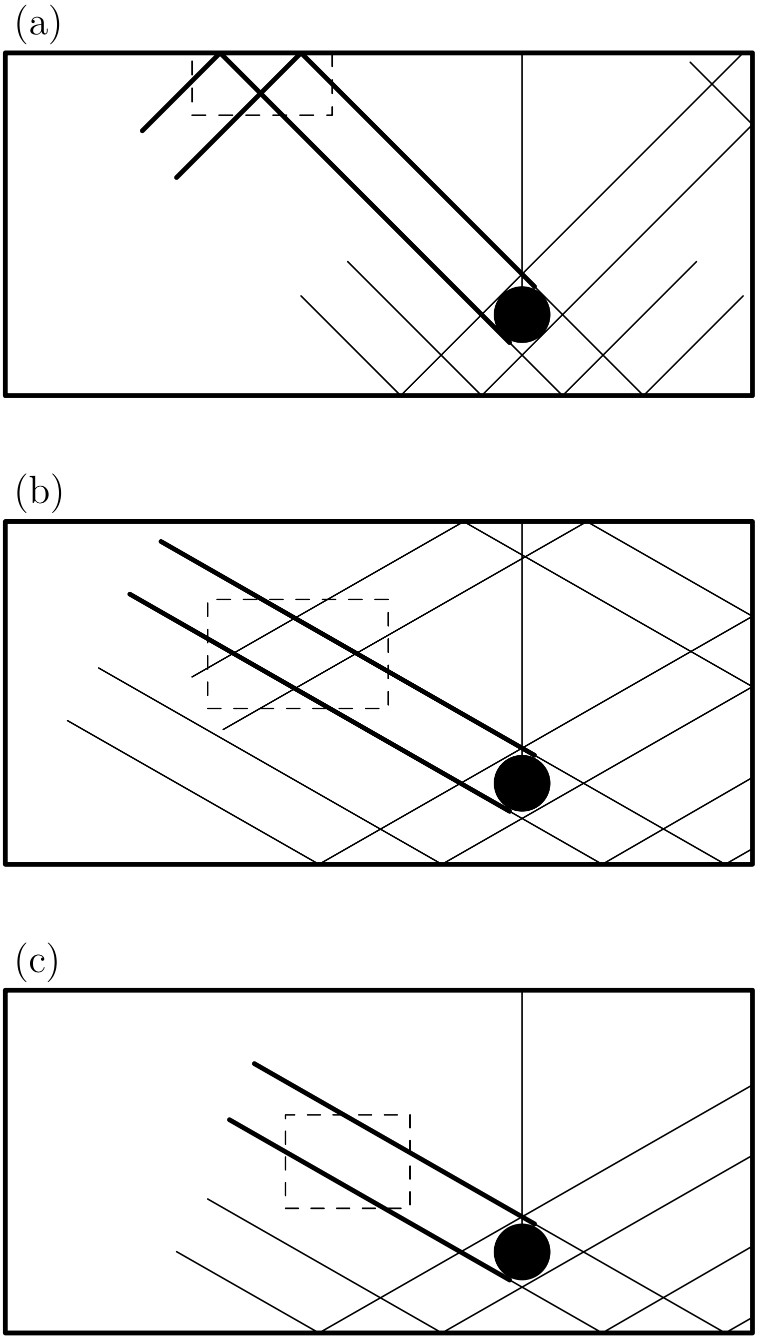

Figure 4.3: Schematic illustration of potential causes for wave breakdown: (a) beam superposition due to surface reflection, (b) beam-beam interference, and (c) breakdown of a freely propagating beam due to instability.

interaction, such as where the primary beam reflects off of the surface, or in a beam-beam interaction that could arise through multiple reflections off of the tank walls and the fluid surface. These situations are depicted in (a) and (b), respectively. We also consider the possibility of the breakdown of a freely propagating, non-interfering primary beam, as shown in (c). Breakdown in a region of beam reflection is the most straightforward to identify from observations because of the proximity to the surface or the bottom of the tank. In the case of beam-beam interactions at mid-depth, we expect that the location of the breakdown would vary significantly according to the wave frequency and the corresponding angle of propagation. Through geometrical considerations, the region of interference would move farther from the position of the cylinder with decreasing forcing frequency.

The greatest insight into the underlying mechanism for the instability has been obtained from a comparison of the breakdown location across experiments, for which the data are plotted in Figure 4.4. The experiments have been separated into upward- and downward-propagating beams in (a) and (b) respectively, with further distinctions made according to the forcing frequency relative to the background buoyancy frequency, as shown by the legend. For reference, we also include lines with slopes predicted by the value of ω_c/N_0, by which we can place approximate bounds on the expected locations of the waves contained in the primary beam at a given frequency. Note that in this qualitative analysis of video footage, the experiments were not restricted to the frequency range that was used for quantitative analyses. In Figure 4.4, a marker indicates the location of wave breakdown for each experiment. We observe that as a group, the markers are displaced somewhat upward in (a) and downward in (b) relative to a line through the centre of the cylinder. This is consistent with our observations from quantitative synthetic schlieren that the primary beam was not centred about the equilibrium position of the

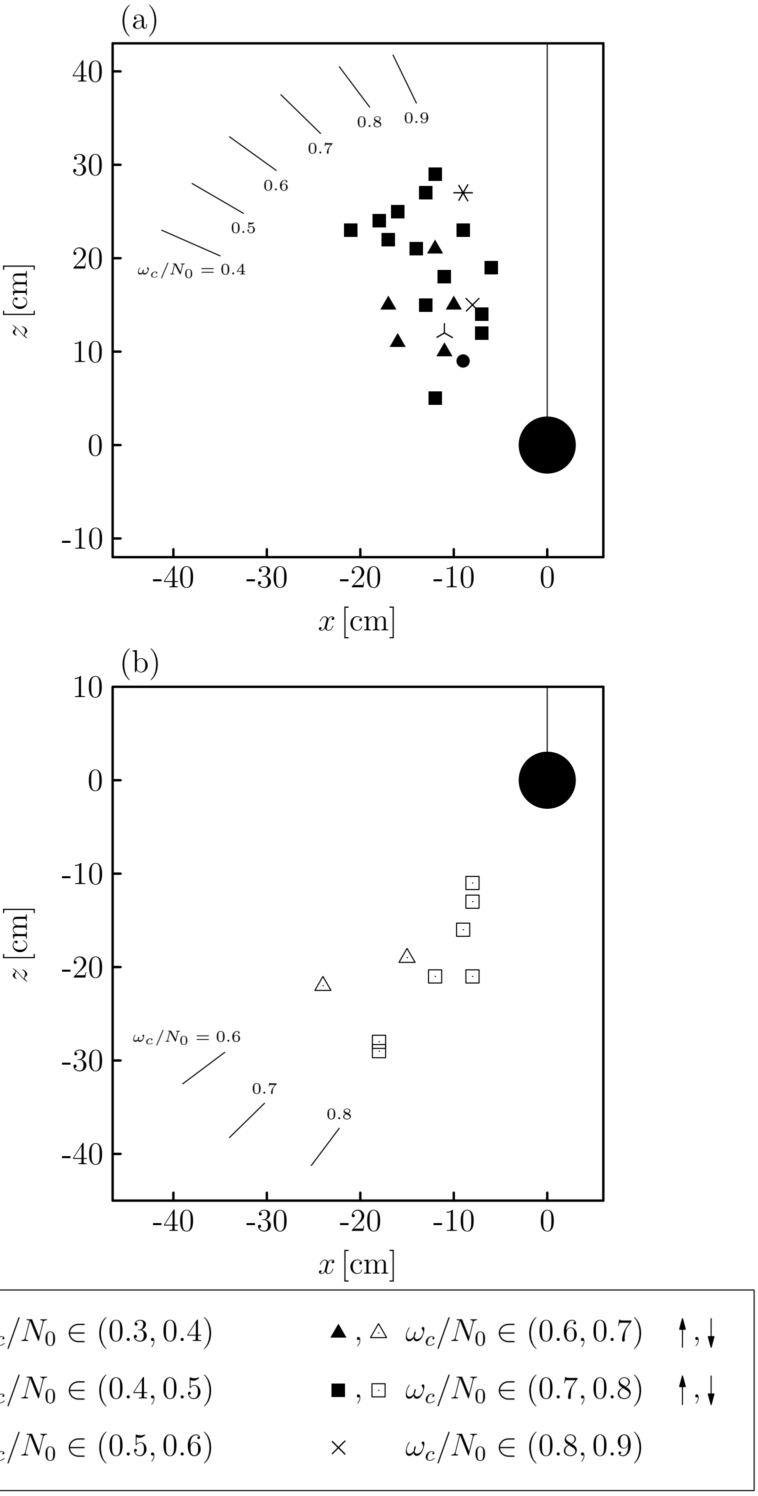

Figure 4.4: Schematic of experimental setup (to scale) with a marker denoting the location of wave breakdown for each experiment as indicated in the legend. Results for upward- and downward-propagating primary beams are shown in (a) and (b), respectively.

cylinder. Therefore, the locations of the markers agree well with our expectations, considering that the primary beam emanates from the turbulent patch. The horizontal coordinates of breakdown were clustered within approximately 20 cm from the centre of the cylinder, and there were no apparent trends in this location based on forcing parameters. The initial wave breakdown according to our criterion occurred at a vertical coordinate that does not correspond to a region of surface or bottom wave reflection, nor does the horizontal distance change significantly with frequency. So, having ruled out beam-beam interactions, we conclude that the waves contained in a single beam undergo a transition to instability independently of interactions with boundaries or other beams. A candidate mechanism for the breakdown of an isolated beam is parametric subharmonic instability, whereby energy is transfered to waves of lower frequency and higher wavenumber than the primary disturbance. This hypothesis provides the motivation for the numerical simulations as described in the following section.

4.4 Parametric Subharmonic Instability

The nonlinear interaction of internal waves through resonant triads was first demonstrated theoretically by Phillips (1960). These resonance conditions provide a mechanism through which energy is transferred between waves of different frequency and wavenumber, such that initially small-amplitude disturbances of the base state may grow in time. A triad of modes with frequencies ω_i and wavenumber vectors $\vec{k}_i$ satisfes the following relations (Staquet and Sommeria, 2002):

$$\vec{k}_1 + \vec{k}_2 + \vec{k}_3 = 0 \tag{4.3}$$

$$\omega_1 + \omega_2 + \omega_3 = 0, \tag{4.4}$$

where both positive and negative frequencies are possible. The dispersion relation for internal waves must be satisfied for each of the wave modes independently.

McComas and Bretherton (1977) describe parametric subharmonic instability (PSI) as a particular class of triad interaction in which energy is transferred from a large-scale primary wave of finite amplitude to two small-scale disturbances with nearly opposite wavenumber vectors. The analysis of Hasselmann (1967) showed that growth is only possible for perturbations of smaller frequency than the primary wave, with the maximum growth rate occurring for the half frequency subharmonic (Staquet and Sommeria, 2002). The amplitudes of the small-scale waves grow exponentially in time with the energy of the primary wave until the wave action density, given by $A_i(\vec{k}_i) = E(\vec{k}_i)/\omega_i$, is approximately equal for each mode (McComas and Bretherton, 1977). Here $E(\vec{k}_i)$ is the energy density per unit wavenumber per unit volume in physical space. This continuing transfer of energy to small-scale disturbances of subharmonic frequencies has significant implications for the evolution of the wave field and has motivated theoretical, numerical and experimental studies of PSI by previous authors.

Mied (1976) performed a linear stability analysis of finite-amplitude plane waves under the Boussinesq approximation. In general, numerical techniques were used to solve the equations to a high accuracy without employing simplifying assumptions about the lengthscales of the growing disturbances. For waves with a wavenumber vector between 10° and 80° from the horizontal, it was found that even those with infinitesimal amplitudes are parametrically unstable. Klostermeyer (1982) improved upon the numerical techniques of Mied (1976) to extend the theory to full generality and confirm that for inviscid flow the most unstable disturbance modes are those with the largest wavenumbers.

Experimental observations of PSI in a cylindrical boundary geometry were presented by McEwan and Robinson (1975). In that work it was also noted that earlier experiments displayed evidence of PSI in shadowgraph images, with the common feature that the appearance of such local instabilities was correlated with the subsequent "irreversible traumatic distortion" of the stratification and finescale layered density discontinuities. In experiments that examined the breaking of standing mode-1 waves in a rectangular tank, McEwan (1983) noted that density microstructure became evident surprisingly rapidly in regions of the tank that were outside of breaking due to PSI. Although the source conditions differ, similar behaviour was observed qualitatively in the oscillating cylinder experiments for the current work. In some cases, widespread visual distortions that were not associated with beam locations appeared in a relatively short time following the breakdown of the primary beam. In more recent experiments, Thorpe (1994) showed the development of parametric instability in an oscillating tilted tube of stratified fluid. Alternating locations of wave overturning were found to correspond with the scale of the subharmonic waves, thereby demonstrating directly that the instability contributes to convective motions and mixing.

Using three-dimensional direct numerical simultions of plane waves in a Boussinesq fluid, Lombard and Riley (1996) investigated the unsteady breakdown of waves to turbulence. It was found that for an initially two-dimensional base wave, there was comparable energy in both the two- and three-dimensional components of the unstable flow. Resonant triad interactions in two dimensions were the dominant mechanism of instability for waves of smaller amplitude, while the three-dimensional character of the breakdown became increasingly prominent for larger base wave amplitudes.

These studies and others have focused on the unstable dynamics of plane waves, whereas the work of this thesis is focused on a quasi-monochromatic internal wave beam. While there exists qualitative shadowgraphic evidence of

PSI in the case of two interacting wave beams (McEwan and Robinson, 1975), no further research on the potential development of PSI for an isolated beam has been conducted. For this reason we have performed numerical simulations to examine the breakdown of a finite-amplitude beam. The details of the simulations and its results are given in the following subsection.

4.4.1 Numerical Simulations

A two-dimensional, fully nonlinear, Boussinesq code was used to simulate the evolution of an internal wave beam. The governing equations in terms of the vorticity, ζ_T, and the total density, ρ_T, are given by (Sutherland, 2006a)

$$\begin{aligned} \frac{D\zeta_T}{Dt} &= \frac{g}{\rho_0}\frac{\partial \rho_T}{\partial x} + \nu\nabla^2\zeta_T, && (4.5) \\ \frac{D\rho_T}{Dt} &= \kappa\nabla^2\rho_T. && (4.6) \end{aligned}$$

Here $D/Dt = \partial_t + u_T\partial_x + w_T\partial_z$ is the material derivative, with the horizontal and vertical components of the total velocity defined as $u_T = -\partial_z\psi_T$ and $w_T = \partial_x\psi_T$. The streamfunction, ψ_T, is related to the vorticity through $\zeta_T = -\nabla^2\psi_T$. In (4.6), ν is the kinematic viscosity and κ is the diffusivity. In practice, the influence of viscosity was determined through the Reynolds number, which was set to correspond with an experimental value for each run of the simulations. The Schmidt number, given by ν/κ, was set to unity for all cases. Although this implies unrealistic values of κ, diffusive processes were not important to the dynamics being studied, as the Reynolds numbers ($\approx 1250 - 1800$) were sufficiently large.

Previous numerical work (Sutherland, 2006b; Brown et al., 2008) has focused on plane waves and spatially localized wavepackets, often with uniform structure in the along-stream direction. The simulations presented here are not an attempt to model accurately all of the characteristics of the oscillating cylinder experiments. Our objective in performing simulations was to investigate potential instabilities in an established beam of finite width. For this study the spatial domain was horizontally and vertically periodic with a resolution of 128 by 512 points in the x and z directions respectively. The code uses finite differencing in the vertical with periodic upper and lower boundary conditions and was run with 64 spectral modes in the horizontal direction. While a horizontally plane wave structure can be resolved with far fewer modes, the finite beam width in the current study means that increased horizontal resolution was required for adequate sampling across the signal.

We have initialized the simulations with a perturbation in the form of plane wave structure in the cross-beam (σ) direction with a Gaussian envelope to determine the beam width. In order to satisfy the doubly-periodic boundary conditions, the full disturbance consisted of a superposition of three identical beams separated by a fixed distance. The beams decayed sufficiently rapidly to prevent an increase in amplitude of the neighbouring beams due to superposition. Given a domain $x \in [0, L]$, $z \in [0, H]$, the beam separation was given by

$$\sigma_s = \frac{LH}{\sqrt{L^2 + H^2}}. \tag{4.7}$$

This distance guarantees the periodicity of the structure by positioning the centre line of the two secondary beams at the appropriate corners of the domain. We have initialized the beams such that the structure resembles the first quadrant of the wave pattern resulting from monochromatic forcing. The centre line of the primary beam was from corner to corner of the domain, regardless of the dimensions L and H. These parameters determine the angle of the beam to the vertical direction, and hence the frequency ω_{igw}, through the relations

$$\Theta = \tan^{-1}\left(\frac{L}{H}\right) = \cos^{-1}\left(\frac{\omega_{\mathrm{igw}}}{N_0}\right). \tag{4.8}$$

The maximum amplitude of the perturbation, cross-beam wavenumber, and standard deviation of the Gaussian envelope, denoted by a_0, k_σ, and σ_0 respectively, are free parameters. The initial structure of the streamfunction is then given by

$$\begin{aligned}\psi(\sigma, t=0) \quad = \quad & a_0 \left\{ \exp\left[\frac{-\sigma^2}{2\sigma_0^2}\right] \cos(k_\sigma \sigma) + \exp\left[\frac{-(\sigma-\sigma_s)^2}{2\sigma_0^2}\right] \cos\left[k_\sigma(\sigma-\sigma_s)\right] \right. \\ & \left. + \exp\left[\frac{-(\sigma+\sigma_s)^2}{2\sigma_0^2}\right] \cos\left[k_\sigma(\sigma+\sigma_s)\right] \right\}. \qquad (4.9)\end{aligned}$$

For each spatial coordinate pair (x, z) in the domain, a transformation to the σ coordinate was performed using $\sigma = -x\cos\Theta + z\sin\Theta$. The value of ψ was calculated for the resulting value of σ according to (4.9), and was then assigned at the original grid point. Small-amplitude randomly generated noise was also superimposed on the field over the entire domain to seed any physical instabilities evenly.

For a beam in the first quadrant, the vertical component of the group velocity is positive. Therefore, in order to obtain the correct signs of the horizontal and vertical wavenumbers k_x and k_z, they were calculated as

$$k_x = |k_\sigma|\cos\Theta, \; k_z = -|k_\sigma|\sin\Theta, \qquad (4.10)$$

where $k_\sigma < 0$.

The parameters that determine the flow were chosen to model the experimental conditions. In all cases, the background velocity was zero and N_0 was the value determined from the density profile, as described in Section 2.2. For a given experiment, the characteristic cross-beam wavenumber, k_σ^*, frequency, ω_{igw}, and vertical displacement amplitude, A_ξ, were known. The initial streamfunction amplitude was determined through polarization relations (Table 3.1) as

$$a_0 = \frac{\omega_{\text{igw}}}{k_x} A_\xi = \frac{\omega_{\text{igw}}}{k_\sigma^* \cos\Theta} A_\xi, \qquad (4.11)$$

such that $a_0 > 0$. The value of A_ξ was determined similarly using the polarization relation (3.6), so the final value of a_0 should be considered an estimate due to the propagation of uncertainties in our experimental measurements. We also have an approximate measure of the beam width from experiments in terms of the parameter α, given by (3.15). For the numerical beam initialization, we have attempted to obtain approximately 2 wavelengths across the width of the beam for consistency with observations and the result that $\alpha \in [1.6, 2.2]$. Contours of the vorticity field are shown at initialization in Figure 4.5(a). Note that the extrema of the contour range are the same for each panel so that direct comparison is possible.

For all simulations that were initialized using parameters comparable to experimental conditions, an instability developed along the central beam after an initial period of regular propagation of phase lines through the beam at a constant angle. The onset of the instability occurred along the centre line of the beam, where the initial amplitude was largest, and the transition appeared visually to occur along the entire length of the beam simultaneously, as shown in Figure 4.5(b). Therefore, we have confidence that the instability is physical and is not caused by boundary effects in the numerical formulation. Within the beam structure, waves began to develop at a larger angle to the vertical direction, and hence a lower frequency, than the initial disturbance. A cascade of energy to smaller scales was also observed. The change in frequency and wavenumber are evident in Figure 4.5(c), where we have superimposed arrows showing the orientation of waves at the initial frequency and the half-frequency subharmonic. The phase lines of the waves including the developed instability align well with the expected direction for the subharmonic, thereby supporting the conclusion that PSI was the primary mechanism for the breakdown of the wave beam in the numerical context. In general, the instability grew in amplitude until overturning began to occur, after which the simulations broke

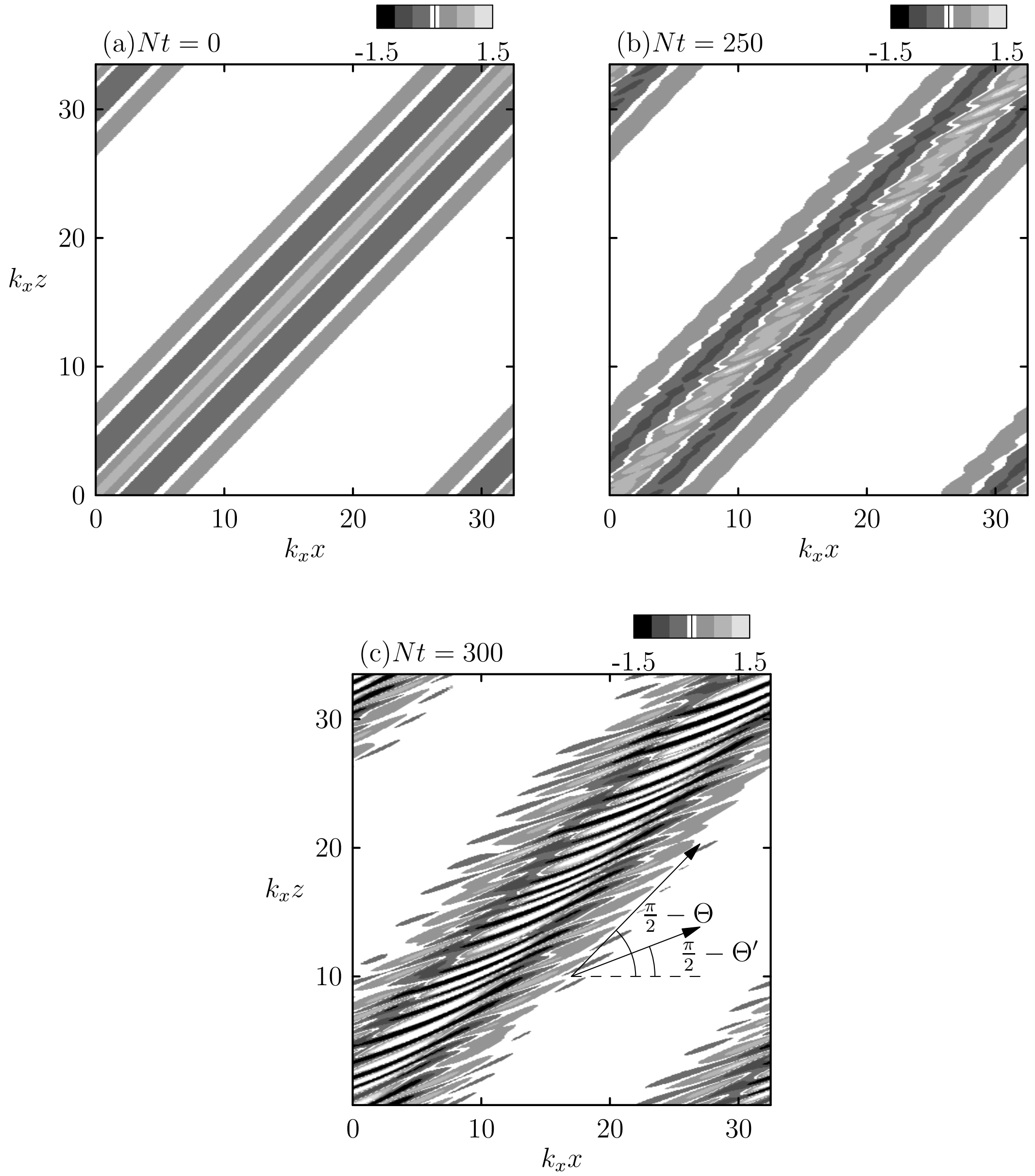

Figure 4.5: Contours of the vorticity, ζ_T [s^{-1}], at (a) initialization, (b) approximately the onset time of the instability, and (c) a late time in the evolution of the wave field. The angles $\frac{\pi}{2} - \Theta = \frac{\pi}{2} - \cos^{-1}(\omega_{\mathrm{igw}}/N_0)$ and $\frac{\pi}{2} - \Theta' = \frac{\pi}{2} - \cos^{-1}(\omega_{\mathrm{igw}}/2N_0)$ are shown in (c).

down rapidly. For waves with smaller initial amplitudes, the simulations ran for the full time of the corresponding experiment. However, the development of PSI was responsible for a complete loss of the coherent beam structure. This effect may explain our observations in raw experimental footage of the sudden spread at late times of large disturbances in the tank that did not correspond with the expected location of beams.

The use of experimentally realistic parameters to initialize the simulations facilitates a comparison between the observed time of PSI onset in the simulations and the experimentally observed time of wave breakdown from the raw schlieren image, as described in Section 4.3.2. Although we cannot specify what physical effects occurred at the time of observation, the hypothesis that PSI arose in the experiments may be supported or refuted through an order-of-magnitude comparison with the results of the simulations. Runs were performed with parameters modelling five characteristic experiments in two different stratifications with a range of forcing frequencies. We have found that the estimated time of the onset of PSI in the simulations differs from the experimental breakdown time by a maximum of a factor of 2. This is reasonable agreement if one considers that the simulations serve to model approximately some of the characteristics of the experimentally measured waves. Using the numerics, we have verified that instabilities became evident in a physically reasonable timescale given realistic input parameters. No systematic pattern emerged in a comparison between the estimated times of instability onset for the numerics and the experiments, e.g. there were cases in which the experimental time was approximately 30% less than the time from simulations and vice versa. The similarity of the experimental and numerical timescales for the development of instabilities serves as support for the hypothesis that PSI was the cause of breakdown of the beams in the experiments.

Chapter 5

Summary and Conclusions

We have studied the generation, propagation, and eventual breakdown of internal wave beams generated by the vertical oscillations of a cylinder in strong stratifications of NaCl or NaI. Large-amplitude forcing caused boundary layer separation around the cylinder, resulting in an oscillatory turbulent source. This generation mechanism was found to influence the characteristics of the internal wave beams in comparison with previous experimental observations and theoretical predictions in the linear regime. Although we did not expect agreement between our observations and theory due to the turbulent and large-amplitude source, the theoretical results were used to illustrate and characterize the effects of the source modification upon the waves.

In order to perform quantitative measurements in fluids with significant density variations with height, a generalized form of synthetic schlieren was developed to take into account the full vertical profile of the density and index of refraction. To implement this technique in the current work, we performed measurements of the index of refraction of NaI solutions as a function of density, over a large range of concentrations. The resulting functional dependence may be used for experiments in which the desired density variations are larger than those permitted by standard NaCl solutions. In this work, the modified synthetic schlieren technique was used to make quantitative measurements of wave frequency, wavenumber, and amplitude.

It was found that the wave frequency was equal to the forcing frequency only for the interval $\omega_c/N_0 \approx 0.5 - 0.8$. For small forcing frequencies, beams were generated at higher harmonics and with larger associated power than the primary beam. With forcing frequencies above N_0, the waves generated by the localized turbulent patch had frequencies of approximately $0.5N_0$. In all cases, the waves with the maximum associated power were observed in the range $\omega_{\mathrm{igw}}/N_0 \approx 0.5 - 0.8$, regardless of the forcing frequency. These results indicate a preferred frequency range that is in agreement with previous work on the turbulent generation of internal waves (Dohan and Sutherland (2003); Aguilar and Sutherland (2006); Taylor and Sarkar (2007)). Wave frequency selection in the typical range occurred despite a dominant frequency component, due to forcing by the cylinder, of the turbulent source. Coherent quasi-monochromatic beam structures were observed emanating directly from the source without an intermediate spatial region of waves with a broad frequency distribution. Therefore differential viscous decay as studied by Taylor and Sarkar (2007) does not account for the observation of frequency selection in this study.

Rather than the cylinder radius, the Ozmidov scale, which characterizes the vertical scale of the eddies in stratified turbulence, was found to be predictive of the size of the turbulent patch surrounding the cylinder and also of the lengthscale of the waves. Also as a consequence of the turbulent generation mechanism, the wave amplitudes were found to be an approximately constant fraction of the horizontal wavelength, which has been noted in previous experimental studies (Aguilar and Sutherland, 2006). However, the magnitude of this ratio differed for experiments in NaCl and NaI stratifications. This observation is currently unexplained and requires further investigation. The measurements of frequency, cross-beam wavenumber and amplitude were combined in a calculation of the power of the primary wave beam. To account for the energy transport by all components of the spectrum, we expressed the power as a sum over wavenumber modes. With this treatment of the full spectrum rather than simply a characteristic lengthscale, the measured wave power was nonetheless found to be approximately an order of magnitude smaller than the rate of energy input. Much of the forcing energy was converted to turbulent kinetic energy in the boundary layer surrounding the cylinder.

Although the experiments were partially motivated by the observation of non-Boussinesq effects in a laboratory setting, the amplitude analysis showed no significant differences between upward and downward propagation of the primary beam. Large-amplitude effects dominated the evolution of the waves. The timescale, and hence vertical scale, over which the waves were steady and quantitatively measurable were insufficient for the observation of asymmetry in the vertical direction.

Qualitative observations from unprocessed videos were used to characterize the time and location of wave breakdown in the experiments. With the motivation of examining potential instabilities for a monochromatic wave beam, fully nonlinear numerical simulations were performed with experimentally realistic input parameters. The results of the simulations showed the development of parametric subharmonic instability at times comparable to the observed values for the experiments. Based on this outcome, we conclude that PSI of the isolated primary beam was responsible for the breakdown of the waves in the experiments at relatively late times. This result contradicts the expectation that nonlinear effects should only be significant in regions of beam self-interaction or collisions.

Bibliography

Aguilar, D. A. and B. R. Sutherland (2006). Internal wave generation from rough topography. *Phys. Fluids 18*, Art. No. 066603.

Brown, G. L., A. B. G. Bush, and B. R. Sutherland (2008). Beyond ray tracing for internal waves. II. finite-amplitude effects. *Phys. Fluids 20*(10). doi:10.1063/1.2993168.

Chan, K. R., L. Pfister, T. P. Bui, S. W. Bowen, J. Dean-Day, B. L. Gary, D. W. Fahey, K. K. Kelly, C. R. Webster, and R. D. May (1993). A case study of the mountain lee wave event of January 6, 1992. *Geoph. Res. Lett. 20*(22), 2551–2554.

Clark, H. A. and B. R. Sutherland (2009). Schlieren measurements of internal waves in non-Boussinesq fluids. *Exp. Fluids 47*(2), 183–194.

Dalziel, S. B. (1992). Decay of rotating turbulence: Some particle tracking experiments. *Appl. Sci. Res. 49*, 217–244.

Dalziel, S. B., G. O. Hughes, and B. R. Sutherland (2000). Whole field density measurements. *Experiments in Fluids 28*, 322–335.

Decamp, S., C. Kozack, and B. Sutherland (2008). Three-dimensional schlieren measurements using inverse tomography. *Exp. Fluids 44*(5), 747–758.

Diamessis, P., J. Domaradzki, and J. Hesthaven (2005). A spectral multidomain penalty method model for the simulation of high Reynolds number localized incompressible stratified turbulence. *J. Comput. Phys. 202*(1), 298–322.

Dohan, K. and B. R. Sutherland (2003). Internal waves generated from a turbulent mixed region. *Phys. Fluids 15*, 488–498.

Fritts, D. C. and M. J. Alexander (2003). Gravity wave dynamics and effects in the middle atmosphere. *Rev. Geophys. 41*, art. no. 1003.

Fritts, D. C. and G. D. Nastrom (1992). Sources of mesoscale variability of gravity waves. Part II: Frontal, convective, and jet stream excitation. *J. Atmos. Sci. 49*, 111–127.

Hasselmann, K. (1967). A criterion for non-linear wave stability. *J. Fluid Mech. 30*, 737–739.

Hurley, D. G. (1997). The generation of internal waves by vibrating elliptic cylinders. Part 1: Inviscid solution. *J. Fluid Mech. 351*, 105–118.

Hurley, D. G. and G. Keady (1997). The generation of internal waves by vibrating elliptic cylinders. Part 2: Approximate viscous solution. *J. Fluid Mech. 351*, 119–138.

Kantha, L. H. and C. A. Clayson (2000). *Small Scale Processes in Geophysical Fluid Flows.* San Diego: Academic Press.

Klostermeyer, J. (1982). On parametric instabilities of finite-amplitude internal gravity waves. *J. Fluid Mech. 119*, 367–377.

Lamb, K. G. (2004). Nonlinear interaction among internal wave beams generated by tidal flow over supercritical topography. *Geoph. Res. Lett. 31*(9). doi:10.1029/2003GL019393.

Lilly, D. K. and P. F. Lester (1974). Waves and turbulence in the stratosphere. *J. Atmos. Sci. 31*(3), 800–812.

Linden, P. F. (1975). The deepening of a mixed layer in a stratified fluid. *J. Fluid Mech. 71*, 385–405.

Lombard, P. N. and J. J. Riley (1996). On the breakdown into turbulence of propagating internal waves. *Dyn. Atmos. Oceans 23*, 345–355.

Makarov, S. A., V. I. Neklyudov, and Y. D. Chashechkin (1990). Spatial structure of two-dimensional and monochromatic internal-wave beams in an exponentially stratified liquid. *Izv. Atmos. Oceanic Phys. 26*, 548–554.

McComas, C. H. and F. P. Bretherton (1977). Resonant interactions of oceanic internal waves. *J. Geophys. Res. 82*, 1397–1412.

McEwan, A. D. (1983). The kinematics of stratified mixing through internal wave breaking. *J. Fluid Mech. 128*, 47–57.

McEwan, A. D. and R. M. Robinson (1975). Parametric instability of internal gravity waves. *J. Fluid. Mech. 67*(4), 667–687.

Mied, R. R. (1976). The occurrence of parametric instabilities in finite-amplitude internal gravity waves. *J. Fluid Mech. 78*, 763–784.

Munroe, J. R. and B. R. Sutherland (2008). Generation of internal waves by sheared turbulence: experiments. *Environ. Fluid Mech. 8*(5-6), 527–534. doi:10.1077/s10652-008-9094-3.

Oster, G. (1965). Density gradients. *Sci. Am. 213*, 70.

Phillips, O. M. (1960). On the dynamics of unsteady gravity waves of finite amplitude. Part 1. The elementary interactions. *J. Fluid Mech. 9*, 193–217.

Rudnick, D. L., T. J. Boyd, R. E. Brainard, G. S. Carter, G. D. Egbert, M. C. Gregg, P. E. Holloway, J. M. Klymak, E. Kunze, C. M. Lee, M. D. Levine, D. S. Luther, J. P. Martin, M. A. Merrifield, J. N. Moum, J. D. Nash, R. Pinkel, L. Rainville, and T. B. Sanford (2003). From tides to mixing along the Hawaiian ridge. *Science 301*(5631), 355–357.

St. Laurent, L. and C. Garrett (2002). The role of internal tides in mixing the deep ocean. *J. Phys. Ocean. 32*, 2882–2899.

St. Laurent, L., S. Stringer, C. Garrett, and D. Perrault-Joncas (2003). The generation of internal tides at abrupt topography. *Deep Sea Res. I 50*(8), 987–1003.

Staquet, C. and J. Sommeria (2002). Internal gravity waves: From instabilities to turbulence. *Ann. Rev. Fluid Mech. 34*, 559–593.

Sutherland, B. R. (2006a). Internal wave instability: Wave-wave vs wave-induced mean flow interactions. *Phys. Fluids. 18*, Art. No. 074107.

Sutherland, B. R. (2006b). Weakly nonlinear internal wavepackets. *J. Fluid Mech. 569*, 249–258.

Sutherland, B. R., S. B. Dalziel, G. O. Hughes, and P. F. Linden (1999). Visualisation and measurement of internal waves by “synthetic schlieren”. Part 1: Vertically oscillating cylinder. *J. Fluid Mech. 390*, 93–126.

Sutherland, B. R. and P. F. Linden (1998). Internal wave generation by flow over a thin barrier. *J. Fluid Mech. 377*, 223–252.

Sutherland, B. R. and P. F. Linden (2002). Internal wave excitation by a vertically oscillating elliptical cylinder. *Phys. Fluids 14*, 721–731.

Tabaei, A. and T. R. Akylas (2003). Nonlinear internal gravity wave beams. *J. Fluid Mech. 482*, 141–161.

Tabaei, A., T. R. Akylas, and K. G. Lamb (2005). Nonlinear effects in reflecting and colliding internal wave beams. *J. Fluid Mech. 526*, 217–243.

Taylor, J. R. and S. Sarkar (2007). Internal gravity waves generated by a turbulent bottom ekman layer. *J. Fluid Mech. 590*, 331–354.

Thomas, N. H. and T. N. Stevenson (1972). A similarity solution for viscous internal waves. *J. Fluid Mech. 54*, 495–506.

Thorpe, S. A. (1994). Observations of parametric instability and breaking waves in an oscillating tilted tube. *J. Fluid Mech. 261*, 33–45.

Thorpe, S. A. (2005). *The Turbulent Ocean.* Cambridge, England: Cambridge University Press.

Voisin, B. (1991). Internal wave generation in uniformly stratified fluids. Part 1. Green's function and point sources. *J. Fluid Mech. 231*, 439–480.

Weast, R. C. (1981). *Handbook of Chemistry and Physics* (62nd ed.). C. R. C. Press.

Appendix A

Review of Theory for Oscillating Cylinder

Here we briefly review the results of Hurley and Keady (1997) for the approximate solution of waves generated by small-amplitude oscillations of a circular cylinder in a viscous Boussinesq fluid. Although our experiments are performed in strongly stratified fluids, the cylinder radius is much smaller than the density scale height, H, so that the wave generation may be considered Boussinesq. Non-Boussinesq effects may modify the amplitude of waves as they propagate away from the source over vertical distances comparable to H. The theory is expected to deviate from our experimental results because it neglects boundary layer separation and the formation of turbulence. However, we use the analytic results as a means for characterizing the experimental observations in terms of an idealized generation mechanism.

A circular cylinder of radius R_c with its central axis aligned in the y-direction is assumed to oscillate vertically with velocity given by the real part of $W\exp(-i\omega_c t)$. This produces two-dimensional waves in the x-z plane. Assuming time-periodic solutions, the wave disturbance field can be characterized by a streamfunction of the form $\psi = \Psi(x,z)\exp(-i\omega_c t)$, so that the fluid velocities in the x and z directions are given by

$$u = -\frac{\partial \psi}{\partial z},\ w = \frac{\partial \psi}{\partial x}\,, \tag{A.1}$$

respectively. With the assumptions that the fluid is uniformly stratified and Boussinesq, that the flow is laminar and that the oscillation amplitude is small in comparison with the cylinder size, the resulting equation for $\Psi(x, z)$ is (Voisin, 1991; Hurley and Keady, 1997)

$$N_0^2 \frac{\partial^2 \Psi}{\partial x^2} - \omega_c^2 \nabla^2 \Psi + i\omega_c \nu \nabla^4 \Psi = 0, \tag{A.2}$$

where ν is the kinematic viscosity and N_0 is the constant buoyancy frequency.

A new coordinate system defines the along-beam coordinate, r, and cross-beam coordinate, σ, for the wave beam propagating upward and to the right of the source in terms of the (x, z) coordinates as

$$\sigma = -x\cos\Theta + z\sin\Theta, \quad r = x\sin\Theta + z\cos\Theta. \tag{A.3}$$

The angle to the vertical, Θ, at which the beam emanates is determined by the forcing frequency relative to the buoyancy frequency:

$$\frac{\omega_c}{N_0} = \cos\Theta. \tag{A.4}$$

This is the dispersion relation under the current assumptions, given that Θ is also related to the wavenumber vector, $\vec{k} = (k_x, k_z)$, through $\Theta = \tan^{-1}(k_z/k_x)$. The boundary-layer approximation (Thomas and Stevenson, 1972) allows one to simplify equation (A.2) in the (σ, r) system by neglecting high-order derivatives with respect to r in comparison with derivatives with respect to σ. The resulting equation is

$$-\frac{\partial^2 \Psi}{\partial\sigma\partial r} + \frac{i\nu}{2\,\omega_c \tan\Theta}\frac{\partial^4 \Psi}{\partial\sigma^4} = 0. \tag{A.5}$$

The viscous no-slip boundary condition on the cylinder is replaced by a free-slip condition under the assumption that the Reynolds number, Re, is large. Equivalently,

$$\lambda = \frac{\nu}{2R_c^2\,\omega_c \tan\Theta} = \frac{1}{2\mathrm{Re}\ \tan\Theta} \ll 1. \tag{A.6}$$

Under these conditions the solution to (A.5) for the wave beam in the first quadrant of the (x, z) coordinate system is given by

$$\Psi = -\frac{iWR_c}{2} e^{i\Theta} \left[\int_0^\infty \frac{J_1(K)}{K} \exp\left(-K^3 \lambda \frac{r}{R_c} - iK \frac{\sigma}{R_c} \right) dK \right], \quad r > 0, \tag{A.7}$$

where J_1 is the first-order Bessel function of the first kind.

Synthetic schlieren measures changes to the background density gradient due to waves. The perturbation is more intuitively quantified as the rate of change of the local squared buoyancy frequency, N_t^2. Thus, for comparison with experiments we will use (A.7) to compute N_t^2 using linear theory (Sutherland and Linden, 2002):

$$N_t^2 \simeq N_0^2 \cos\Theta \sin\Theta \frac{\partial^2 \Psi(r, \sigma)}{\partial \sigma^2}. \tag{A.8}$$

Thus from (A.7), we obtain

$$N_t^2 = \frac{iW}{2R_c} e^{i\Theta} N_0^2 \cos\Theta \sin\Theta \left[\int_0^\infty K J_1(K) \exp\left(-K^3 \lambda \frac{r}{R_c} - iK \frac{\sigma}{R_c} \right) dK \right]. \tag{A.9}$$

At any distance, r, from the cylinder centre, the across-beam structure can be computed from (A.9) using Fast Fourier Transforms. Figure A.1 shows the transition in the cross-beam structure with increasing distance from the cylinder. In (a), a beam cross-section in the near field reveals bimodal waves, whose amplitude envelope peaks near tangents to the cylinder. The far field profile becomes unimodal, as shown in (b), with the peak in amplitude along a line through the cylinder centre.

Because the theory assumes flow around the cylinder is laminar and free-slip, it underestimates the experimentally observed beam width. For moderate-amplitude forcing, an estimate of the thickness of the viscous boundary layer surrounding the cylinder accounts for the expected discrepancy between the theoretically predicted beam width and the experimentally observed value

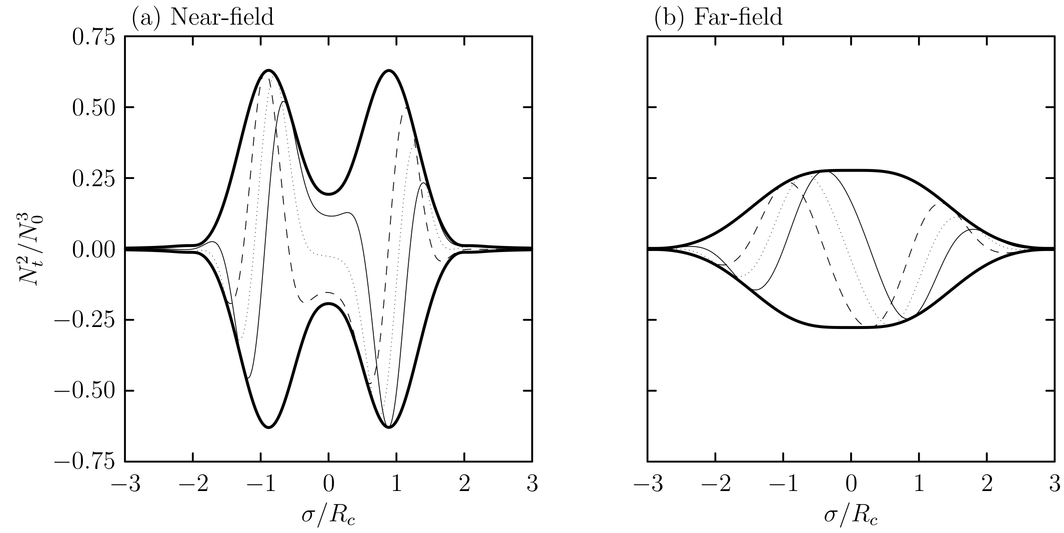

Figure A.1: Normalized N_t^2 field as a function of normalized cross-beam coordinate, calculated from (A.9). The heavy solid curves are the amplitude envelope over one wave period, and the inner curves show the field at particular values of the phase.

(Sutherland et al., 1999). In our experiments the forcing amplitude is on the order of the cylinder radius so that a thick turbulent layer develops around the cylinder. This causes many of the assumptions made in the derivation of (A.9) to break down. A calculation of the viscous boundary layer thickness alone significantly underestimates the expected discrepancy between theoretical predictions and observations.

Appendix B

Derivation of Synthetic Schlieren Equations

Synthetic schlieren is an optical measurement technique that depends upon the variation of the index of refraction of a fluid with density. In laboratory experiments with stratified fluids, propagating internal waves cause density perturbations in space and time that can be visualized through the apparent displacement of an image behind the tank. Synthetic schlieren allows one to compute the internal wave field from measurements of the visual distortions of this image. The application of schlieren to fully three-dimensional flows using inverse tomography has been developed recently by Decamp et al. (2008) and demonstrated through numerical experiments. Here we review the derivation of the synthetic schlieren method for two-dimensional flows, as presented by Sutherland et al. (1999). We focus on the technique as it was implemented in previous studies, i.e. in a Boussinesq stratification with buoyancy frequency N. The results are restricted to the case of fluid disturbances in the (x, z) plane, such that the properties of the flow are uniform in the y (cross-tank) direction. Previous experiments and the work presented in this thesis were designed to satisfy this physical condition.

The path of a ray of light as it passes through a stratified fluid varies

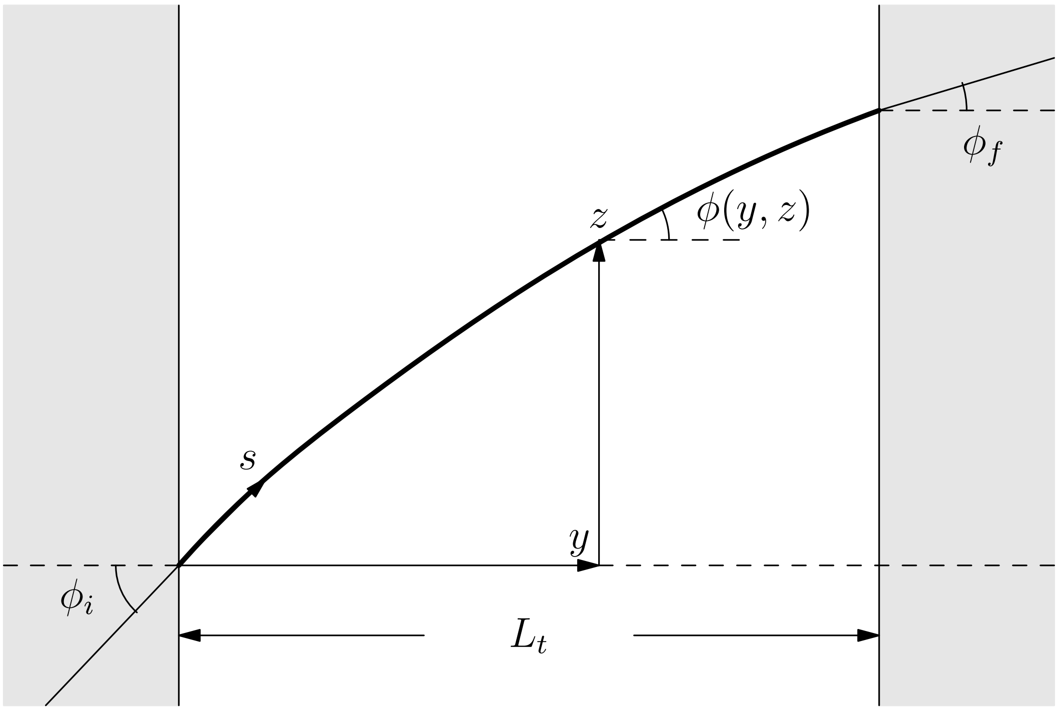

Figure B.1: Schematic diagram of a close-up view of the stratified fluid bounded by tank walls, which are represented by the shaded areas. The angle of incidence and curvature of the path are exaggerated for clarity.

according to Snell's Law,

$$\bar{n}\cos\phi = \text{constant.} \tag{B.1}$$

Here $\bar{n}(x, z)$ is the index of refraction of the fluid and $\phi(y, z)$ is the angle of the ray to the surfaces of constant $\bar{n}$, which are horizontal in the undisturbed state. The path is decomposed into coordinates parallel (y) and perpendicular (x or z) to these isosurfaces. For simplicity and consistency with the current study and previous experiments, we will restrict the derivation to the optical tracking of vertical displacements only and focus on z as the perpendicular coordinate. In this case, the image consists of a pattern of alternating horizontal black and white lines that are uniform in the x direction. The path of the ray through the fluid under these assumptions is shown schematically in Figure B.1. Denoting the along-path coordinate as s, we differentiate (B.1) with respect to s and use the geometric relations $dy = ds \cos\phi$ and $dz = ds \sin\phi$ to obtain

$$\frac{d\bar{n}}{ds}\cos\phi - \bar{n}\sin\phi\,\frac{d\phi}{ds} = \frac{\partial\bar{n}}{\partial z}\cos\phi\sin\phi - \bar{n}\sin\phi\,\frac{d\phi}{ds}. \tag{B.2}$$

Noting that

$$\frac{d^2z}{dy^2} = \frac{d}{dy}(\tan\phi) = \frac{\partial s}{\partial y}\frac{d}{ds}(\tan\phi) = \sec^3\phi\,\frac{d\phi}{ds}, \tag{B.3}$$

we may eliminate $d\phi/ds$ in (B.2), resulting in

$$\frac{d^2z}{dy^2} = \frac{\sec^2\phi}{\bar{n}}\frac{\partial\bar{n}}{\partial z}. \tag{B.4}$$

The density gradient is introduced through the following substitution:

$$\frac{\partial\bar{n}}{\partial z} = \frac{d\bar{n}}{d\bar{\rho}}\frac{\partial\bar{\rho}}{\partial z} = -\left(\frac{1}{g}\frac{\rho_0}{n_0}\frac{d\bar{n}}{d\bar{\rho}}\right)n_0N^2, \tag{B.5}$$

so that

$$\frac{\partial\bar{n}}{\partial z} = -n_0\gamma N^2, \tag{B.6}$$

where

$$\gamma = \frac{1}{g}\frac{\rho_0}{n_0}\frac{d\bar{n}}{d\bar{\rho}}. \tag{B.7}$$

Here ρ_0 and n_0 are reference values of the density and index of refraction. In a Boussinesq stratification it is sufficient to treat γ as a constant over the entire tank depth because of the small variation in the fluid properties with z. For solutions of NaCl, the value of $d\bar{n}/d\bar{\rho}$ may be obtained from tables, such as those in Weast (1981). (B.4) is simplified by the assumption that the angle of incidence of the ray to the horizontal is small, which is guaranteed by the positioning in space of the experimental apparatus. Using (B.6) and assuming that $\sec^2\phi \simeq 1$, we obtain

$$\frac{d^2z}{dy^2} = -\gamma N^2. \tag{B.8}$$

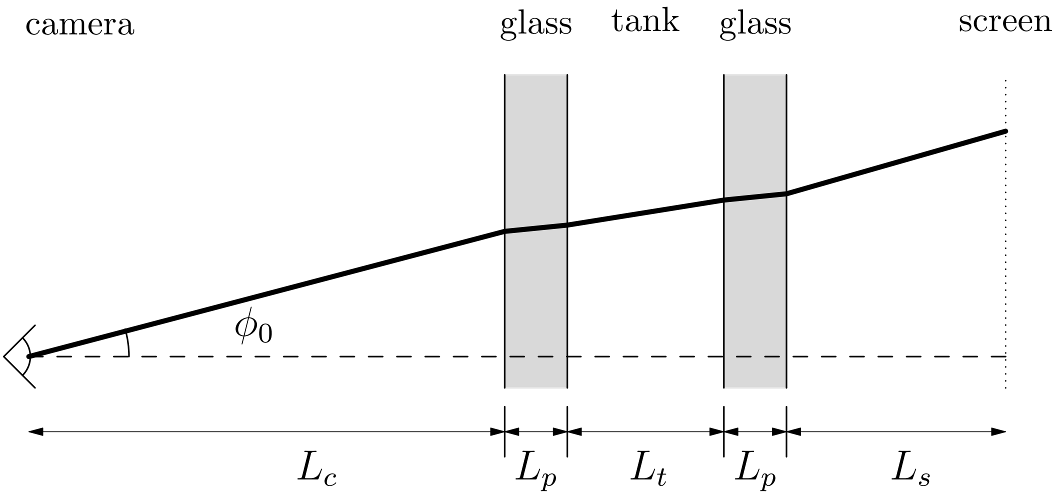

Figure B.2: Schematic diagram (not to scale) of a typical experimental apparatus for synthetic schlieren, with the path of a light ray represented by the solid line.

Integrating this equation yields the path of the light ray, $z(y)$, as it traverses the span of the tank:

$$z(y) = z_i + y \tan \phi_i - \frac{1}{2}\gamma N^2 y^2, \tag{B.9}$$

where z_i and ϕ_i are the vertical coordinate and the angle to the horizontal at the point of incidence of the ray. The stable stratification causes the light to follow a parabolic path through the fluid, thereby changing the angle, ϕ_f, at which the ray meets surfaces of constant $\bar{n}$ upon exiting the tank.

For experimental applications, the light rays pass through several interfaces between different media on their path from the screen to the camera, as shown schematically in Figure B.2. To obtain the total vertical deflection of a ray between these endpoints, Snell's Law is applied at each interface with the corresponding index of refraction for each medium. Performing this calculation and assuming that each angle of incidence is small, such that $\tan \phi_i \simeq \phi_i$, the total vertical deflection for a ray entering the camera at an angle ϕ_0 above the horizontal is given by

$$\begin{aligned} z(N^2, \phi_0) \;\simeq\; & L_c\phi_0 + L_p(n_a/n_p)\phi_0 + L_t(n_a/n_w)\phi_0 - \frac{1}{2}\gamma N^2 L_t^2 \\ & + L_p(n_a/n_p)\phi_0 - L_p(n_w/n_p)\gamma N^2 L_t + L_s\phi_0 - L_s(n_w/n_a)\gamma N^2 L_t. \end{aligned} \tag{B.10}$$

The lengths L_c, L_t, L_p and L_s are shown in Figure B.2, with the subscripts referring to the camera, tank, walls and screen, respectively. Tank walls are typically constructed of Perspex acrylic, with the index of refraction denoted as n_p. The constants n_a and n_w refer to the indices of refraction of air and water, respectively. The use of the constant n_w for the entire stratification is a result of the Boussinesq approximation.

When internal gravity waves are present in the tank, the local value of N^2 changes with the perturbation to the background stratification. One may calculate the apparent displacement, Δz, of the image due to internal waves by substituting $N^2 \rightarrow N^2 + \Delta N^2$ in (B.10), which yields

$$\Delta z(\Delta N^2, \phi_0) \simeq -\frac{1}{2}\gamma \Delta N^2 L_t^2 - L_p(n_w/n_p)\gamma \Delta N^2 L_t - L_s(n_w/n_a)\gamma \Delta N^2 L_t. \tag{B.11}$$

Finally, since Δz is measured experimentally in order to determine the wave field, we rearrange the above equation to solve for the perturbation to the squared buoyancy frequency in terms of known quantities:

$$\Delta N^2 \simeq -\Delta z \, \frac{1}{\gamma} \left[\frac{1}{2} L_t^2 + L_t \, n_w \left(\frac{L_p}{n_p} + \frac{L_s}{n_a} \right) \right]^{-1}. \tag{B.12}$$

The calculation of Δz from experimental images is based upon tracking the changes in light intensity recorded at each pixel in the field of view of the camera. For successive frames, the apparent displacement is calculated if the contrast in intensity across three pixels is greater than an explicit threshold value. For details on the implementation of synthetic schlieren, the reader is referred to Sutherland et al. (1999).